UH-60A Rotor and Coupled Rotor-Fuselage Simulation Framework Validation and Analysis

Willem Rex [*] Tobias Pflumm [†] Manfred Hajek [‡]

Institute of Helicopter Technology
Technical University of Munich, 80333 Munich, Germany

In helicopter engineering advanced simulation means are available today which allow to run analysis and optimization tasks using modern computational capabilities [1–7]. In this context it is important to demonstrate the validity of the simulation model and the simulation approach by comparison with experimental data. This work establishes a validated reference model similar to the UH-60A for research activities on rotor blade design and analysis of rotor-fuselage coupling mechanisms. The focus is on structural representation. Literature is reviewed for data to define and validate the model. Main rotor performance and structural characteristics are in good agreement with the experimental data. Two independently established modal fuselage representations are mutually consistent and agree with literature at lower but not at higher frequencies. Coupled rotor-fuselage simulations show reasonable results compared to test data. However, the approach does not represent experimental mean half peak-to-peak hub accelerations exactly.

Nomenclature

AEFA	Aviation Engineering Flight Activity
API	application programming interface
COG	center of gravity
DOF	degree(s) of freedom
DAMVIBS	Design Analysis Methods for Vibrations
HOGE	hover out of ground
LRTA	large rotor test apparatus
MAC	modal assurance criterion
MSF	modal scale factor
MTRA	Modern Technology Rotor Airloads (Program)
NFAC	National Full-Scale Aerodynamic Complex
P/DB	plot database
RBM	rigid body mode(s)
RMS	root mean square
RSIS	Rotorcraft Systems Integration Simulator
RSRA	Rotor System Research Aircraft
TPP	tip path plane
UTTAS	Utility Tactical Transport Aircraft System
$g\,[\mathrm{m\,s^{-2}}]$	acceleration of gravity
$\tilde{m}_k$	modal mass of mode k
N_b	number of rotor blades
$\Omega\,[\mathrm{rad\,s^{-1}}]$	rotor angular velocity
x, y, z	cartesian coordinates
$\overline{(.)}$	mean

[*] Graduate Research Assistant, willem.rex@tum.de
[†] Graduate Research Assistant, tobias.pflumm@tum.de
[‡] Professor and Department Head, hajek@tum.de

Presented at the 45th European Rotorcraft Forum, Warsaw, Poland, 17-20 September, 2019.

Introduction

Increasingly, simulation plays an important role in modern rotorcraft design to further improve aircraft performance, efficiency, envelope and vibrations. Advanced simulation means that cover the high structural non-linearities and the complex aerodynamic as well as aeroelastic characteristics are available today and the understanding of related effects has greatly developed [8]. In conjunction with advanced computational resources this allows to use simulation tools for prediction and optimization. However, it is inevitable to validate simulation models against experimental data to ensure its correctness and to understand its shortcomings.

The aim of this work is to establish a validated helicopter model similar to the UH-60A [9, 10] with focus on the structure which is meant to serve as a reference at the Institute of Helicopter Technology for different types of scientific investigations. It is intended to use the model for the analysis of structural loads, vibrations and instabilities, ground and air resonance as well as for design and optimization of rotor blades, other structural components and morphing structures.

The UH-60A is a twin engine single main rotor utility helicopter with a maximum takeoff weight of approximately 10.5 tons, which was first flown in 1974 and developed in context of the UTTAS program [9, 10]. The UH-60A is chosen as reference due to the extensive amount of available data and due to numerous former research activities which are based on the UH-60A. This helicopter serves still today as an important reference for validation [11, 12]. However, available data is often both required to be compiled to match the software input and distributed among several reports and publications. In this work literature is

reviewed with focus on data to setup a UH-60A coupled rotor-fuselage environment and data for its validation. The established validated models are described in detail and all information about the geometry, the structural properties as well as the aerodynamic properties are given herein.

In the context of the U.S. Army Aviation Engineering Flight Activity (AEFA) several flight tests have been conducted with different versions of the UH-60A. From 1979 to 1980 two UH-60A of the first year production generation have been flight tested to determine performance, vibrations and handling qualities [13]. To update the test results two UH-60A, one of first and one of six year production generation have been flight tested from 1983 to 1984 [14]. To obtain additional data and to support the Modern Technology Rotors Airloads (MRTA) program a six year production generation aircraft has been flight tested in 1987 [15]. In 1988 again a UH-60A of 12th year production generation was flight tested to update the flight test database [16]. Data observed from the AEFA program was used to establish and validate a flight physics model [17–19] for implementation on the Rotorcraft Systems Integration Simulator (RSIS) [20].

In the context of the MTRA program or short Airloads Program [21] full scale flight tests have been conducted from 1993 to 1994 [22–24]. The modal characteristics of the experimental MTRA configuration baseline rotor blades and as well as the instrumented blades were experimentally quantified [25]. One principle objective of the Airloads Program was the characterization of rotor fuselage coupling phenomena [26]. Note that a consistent mistake in the MTRA data was discovered for results that are published before 2005 and which are related to rotor azimuth position [27]. Trim target values used in this work like roll and pitch shaft moments are affected which have been measured in the rotating domain [23,27]. Correspondingly, affected data is corrected in this work by rotating the properties noted in the shaft frame S (see figure 2) using equation 1.

$$\begin{pmatrix} {}_Sx \\ {}_Sy \end{pmatrix}_{corr} = \begin{pmatrix} \cos(14°) & -\sin(14°) \\ \sin(14°) & \cos(14°) \end{pmatrix} \cdot \begin{pmatrix} {}_Sx \\ {}_Sy \end{pmatrix}_{err} \quad (1)$$

The Rotor System Research Aircraft (RSRA) which was equipped with three different rotor systems based on the UH-60A rotor served as an experimental aircraft to gain insights into rotor mechanics and to conclude design guidelines and to identify design drivers of modern helicopter rotors [28]. Where data is not explicitly available for the UH-60A, original UH-60A components included in the RSRA aircraft are used in this work as reference [28].

To support flight tests, full-scale wind tunnel experiments with a UH-60A rotor have been conducted in the National Full-Scale Aerodynamic Complex (NFAC) 120x80ft and 80x40ft wind tunnels [29–31]. In both wind tunnels the original UH-60A fuselage was removed and the rotor was mounted on top of the Large Rotor Test Apparatus (LRTA) [32].

In the past, experiments have been conducted to identify the elastic fuselage characteristics of the UH-60A. In the context of the DAMVIBS program Sikorsky conducted UH-60A fuselage shake tests [33, 34]. An empty baseline production UH-60A fuselage without significant modifications with fixed absorbers was used and 50% of the rotor blade mass was considered. Subsequently, masses for the pilot, copilot, equipment, fuel and flight test instrumentation was added to the configuration to mimic the flight tested AEFA configuration and the shake tests have been repeated [34]. Both configurations were in addition modeled using finite element methods [33–35]. A third configuration with different modal characteristics is the helicopter flown during the MTRA program [26]. A finite element representation of the MTRA configuration was established based on the NASA/AEFA model [26]. A third corresponding ground shake test study with a MTRA configuration was originally scheduled at NASA Ames for 1995 [26], however no related published test data is found for the analysis. Before the DAMVIBS Program, which started in 1984, at least the UH-60A main rotor head has been shake tested [36, 37]. Herein, the model is referred to as *HUBNODE* configuration. However, references of the tests can not be traced back in the reviewed literature, hence the test setup is not evident.

Since the fuselage is important to be considered in optimization and analysis of vibrations and instabilities [8,38–43] and since the hub fixed simulation of a helicopter rotor does not resolve vibrations appropriately [44–46] the rotor model is supplemented with a fuselage representation which can be tightly coupled with the rotor. The rigid motion of the fuselage is discussed as well since its motion has a significant effect on vibrations [47, 48]. However, even with advanced simulation means the prediction of vibrations prior to the first flight is still difficult today [8]. In coupled rotor fuselage analysis the level of vibrations is significantly affected by the modal representation of the fuselage [40] which in turn are highly affected by the load and balance of the fuselage [17, 26]. In addition, finite element modeling of a helicopter fuselage does often not agree reasonably with test data [26, 33–35]. In regard to this it is intended to establish a reasonable fuselage representation based directly on experimental data rather than to replicate reference characteristics exactly.

After the models of the rotor and the fuselage are established they are coupled and the calculated hub accelerations are compared to reference data. Possible shortcomings in the modeling approach and suitable countermeasures are discussed based on the discrepancies found during the validation. However, no fundamental analysis on the exact coupling mechanisms will be presented in this context.

Methodology

The helicopter rotor model is simulated using *Dymore* [49], a software for the simulation of multibody systems which

features one and two dimensional finite element representations, helicopter specific aerodynamic models and incorporates means for parallelization [50]. In the past *Dymore* was used in the context of wind turbine simulation [51–53], structural analysis of tilt-rotors and active flaps [54–57] as well as helicopter structural optimization, morphing and adaptive structures [1–7, 58, 59]. Coupled UH-60A rotor-fuselage investigations have been conducted with *Dymore* [46, 60] and UH-60A pitch link loads have been validated against Airloads Program data using *Dymore* as well [61]. For improved UH-60A rotor loads predictions previous studies used both coupled *Dymore*-Free-Wake and coupled *Dymore*-CFD approaches [62–74].

Multiple ways exist to realize coupled rotor fuselage analysis. An approach was used in the past which is referred to as *impedance matching* [36, 40, 75]. To correct hub fixed simulation for the actual motion of the hub, impedance matrices for the rotor and the fuselage are used [39, 76, 77]. In this work *impedance matching* is not used because the calculation of the required matrix is cumbersome for the nonlinear rotor representation used herein and the matrix depends on advancing ratio [39]. Another way is the formulation of rotor and fuselage equations in one set of equations [78, 79]. If parts of the model are represented by generalized coordinates this is called *mode synthesis*. Among other approaches, *mode synthesis* has been previously realized for rotor fuselage coupling using Hertings method [12, 46].

In this work the coupled analysis of both models is achieved by an exchange of forces and displacements in each time step which is realized by iterating the equations 2 and 3. First, starting from a time step i, the main rotor shaft forces are calculated at the connection node of the rotor and the fuselage for a time step $i+1$ using *Dymore*, see equation 2. Second, the fuselage response is calculated according to equation 3 using a fourth order Runge-Kutta time integration scheme. The displacements are then prescribed in the next time step of the rotor simulation and again corresponding forces are calculated [42, 80].

$$\mathbf{F}_{i+1,\mathrm{mr}} = f_{\mathrm{rotor}}\left(\mathbf{x}_{i,\mathrm{mr}}\right) \tag{2}$$

$$\mathbf{x}_{i+1,\mathrm{mr}} = f_{\mathrm{fuselage}}\left(\mathbf{F}_{i+1,\mathrm{mr}}\right) \tag{3}$$

The solution is iterated over 20 rotor revolutions to observe a periodic state. Then, in periodic conditions 20 main rotor revolutions are calculated. For comparison a hub fixed coupling approach is realized as well by keeping all displacements $\mathbf{x}_{i,\mathrm{mr}}$ at zero during the calculation of the rotor response. The interface to couple *Dymore* with the external fuselage model is realized using a wrapper for *Dymore* as illustrated in figure 1. The *Dymore* source code is compiled into a library, which requires still the same input model definition files as the standalone *Dymore* version. However no output files are generated during the execution, instead all required data is passed to the *Python* interface. The interface is established using an API which is provided by the *Dymore* library. The API contains all required functions for data exchange and for control of the simulation process. The API is wrapped to congruent *Python* functions which can be called from a *Python* environment. A similar approach in realized in *RCOTOOLS* for *CAMRAD II* and was used in the past for CFD coupling with *Dymore* [67]. Others compiled the external code into the *Dymore* source code [64]. However, the most often used approach is to use file input/output [66, 69, 72]. The advantage of the approach used herein is that time consuming file input/output operations are avoided. In addition, the model representation in memory is only established once at the beginning of the job and not each time the standalone executable is called. Access to the data objects in memory gives more flexibility for optimization and even morphing structures can be realized, since properties can be changed during runtime in each iteration step.

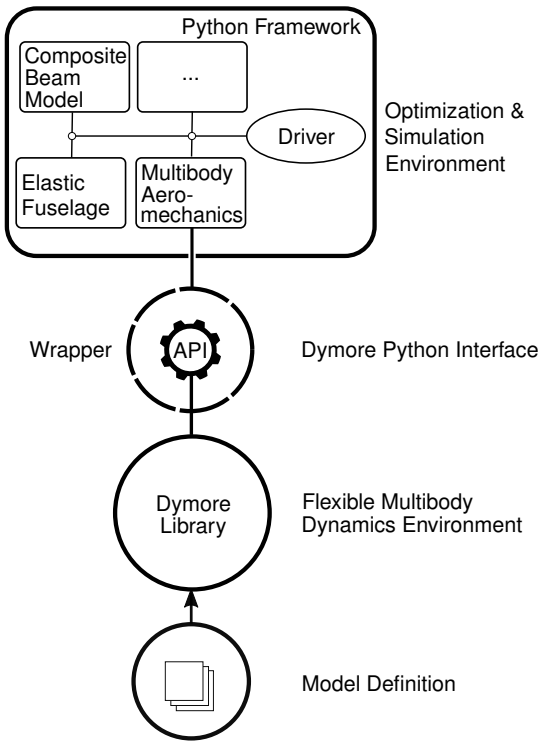

Fig. 1: Interface & simulation framework for coupled rotor fuselage analysis and structural optimization.

Rotor Model

The multibody representation of the rotor in the reference configuration is shown in figure 2. This configuration agrees with the P/DB reference orientation [27]. A similar model has already been established in *Dymore* previously [49]. For clarity reasons, only one of four assemblies ($N_b = 4$) equally distributed in azimuthal direction is depicted in figure 2, consisting of the rotor blade, rotor blade attachment, pitch link, lag damper and bifilar absorber. Accordingly, only one quarter is depicted of the swash plate

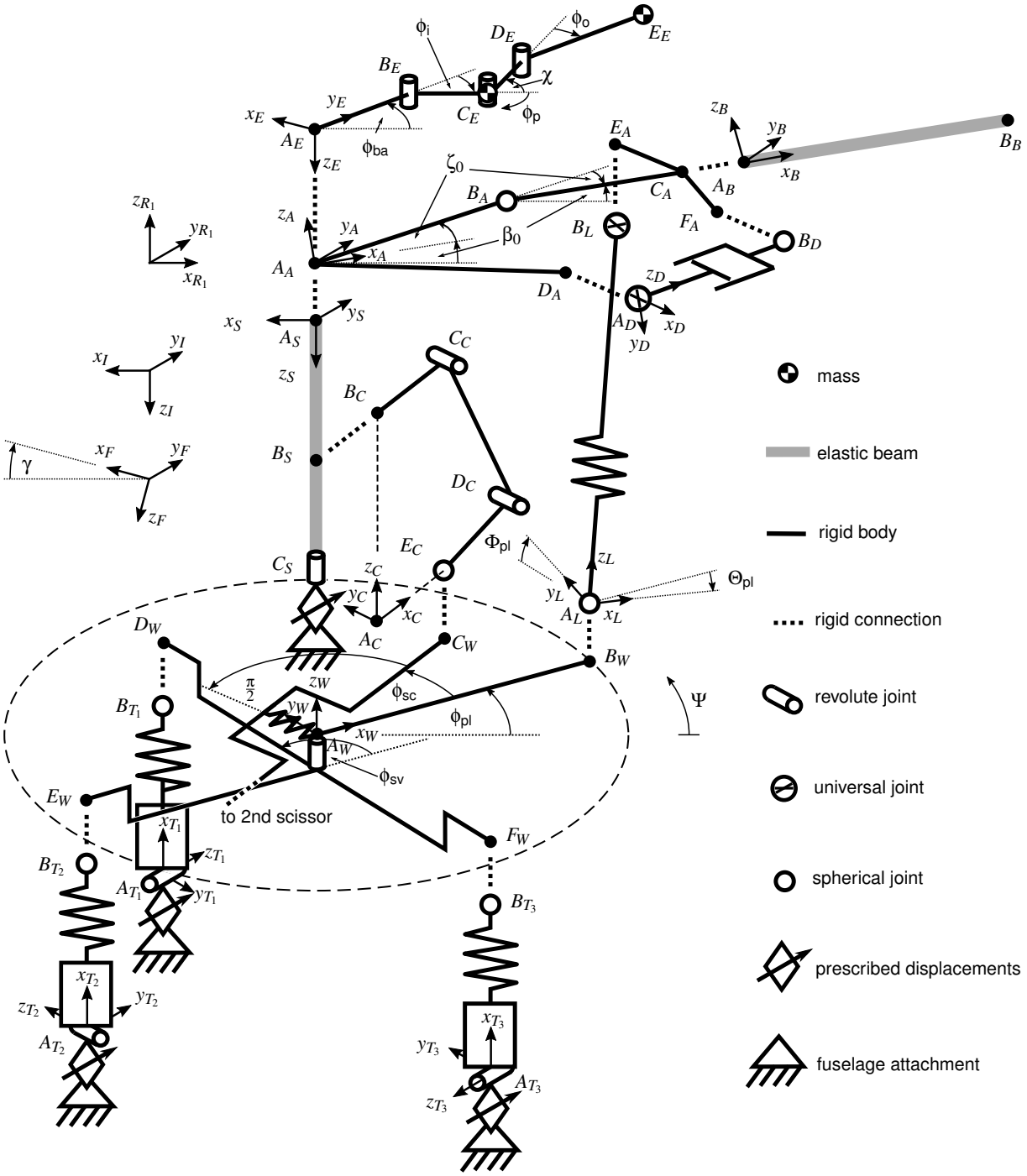

Fig. 2: Multibody representation of the UH-60A main rotor system. Only one of four blades and one of two scissors depicted. Coordinate systems and geometry are defined in figure 8 and table 4.

and the rotor head. The quarter assemblies have identical properties, including the blades. The attachment includes the blade retention, the rotor head, the elastomeric bearing as well as the damper horn and the pitch horn. To replicate the geometry and the properties of the quarter assembly the intermediate frames $R_i, i = [1,2,3,4]$ are introduced, see figure 8. The frame R_1 is depicted in figure 2. In addition only one of two scissors is depicted. The second scissor is shifted 180° in azimuthal direction. The intermediate frame R_3 is used to replicate the scissors' geometry. Another intermediate frame F is given to align the fuselage, which is tilted about the shaft angle γ. Hence, the rotor shaft is aligned with the z_I axis in which direction the gravitational field is acting.

The geometry is defined by the coordinates of all points and angles indicated in figure 2 following a simple logic. All points are measured in its individual local body-frame coordinates, since they are typically given as such in liter-

ature rather than measured in inertial coordinates. The definition of each body-frame is likewise given using its unit vectors $\vec{e}_2$ and $\vec{e}_3$ measured in its individual parent system. Note that the point A is always located at the origin of the corresponding local frame and that the frame is defined by a right-handed orthonormal base, thus it holds $\vec{e}_1 = \vec{e}_2 \times \vec{e}_3$. The reference coordinate system of all points and unit vectors is indicated by a subscript in figure 2. Figure 8 indicates the relationships of all coordinate systems and locations of all points which are indicated in figure 2. In addition, all geometric constants used in figure 8 are listed in the table 4 together with all relevant references where the data is found.

At four points the model is attached to the fuselage via revolute joints namely the rotor shaft and the three servos. The servos can be actuated in local x-direction and feature an elasticity, represented by a one dimensional linear spring element. The servos are connected to the non-rotating part of the swash plate via spherical joints to establish isostatic conditions. The rotor shaft is represented by eight finite beam elements with linear shape functions. Four elements are equally distributed between A_S and B_S and four are equally distribute respectively between B_S and C_S. At its top, the shaft is attached to the main rotor hub. The main rotor hub is a rigid body and features a coning angle β_0 and a structural pre-lag angle ζ_0 which are both graphically illustrated in ref. [81] and considered to establish the correct flap and lag angle for zero strain in the reference configuration of the elastomeric bearing, which is located at point B_A [82].

The flap, lead-lag and feathering hinge are assumed to be located in one identical point [36]. The elastomeric bearing establishes the flap, lead-lag and feathering motion and connects the blade retention to the rotor hub. The blade retention is modeled as a rigid body and provides itself connections for the pitch link, lag damper and the rotor blade. The rotor blade is represented by 14 finite beam elements of linear shape functions which are equally distributed. The blade is rigidly attached to the rotor retention. The beginning of the blade is at $0.1R$ [83]. The lag damper features a one dimensional nonlinear damper characteristic and is connected to the damper horn using a spherical joint and to the rigid rotor head via a universal joint. The connection at D_A is assumed to be in the precone plane (x_A-y_A-plane). Calculations show that this assumption is correct with $1e^{-3}$m accuracy. However, it simplifies the geometrical definition noticably. The pitch link features a one dimensional linear spring. One half of its mass is located at point A_L the other half is located at B_L. The lower point of the pitch link is connected to the pitch horn using a universal joint and to the rotating part of the swash plate via a spherical joint. The rotation of the swash plate is established by a revolute joint. All other components of the swash plate are rigid bodies. The mass of the swash plate is located at point A_W. The inertia of the swash plate about the y_W- and x_W-axis are considered as well. The two scissor pickups at the swash plate are connected to a spring. The purpose of this spring is to establish an additional degree of freedom and an equivalent dedicated stiffness, since the scissors can otherwise cause unrealistic displacements of the shaft. In this work the stiffness of this spring equals zero. The rotating part of the swash plate is connected to the scissor via a spherical joint. The scissor itself consists of rigid bodies connected by two revolute joints. The point B_C is rigidly connected to the rotor shaft.

The bifilar absorber is mounted on top of the rotor assembly, rigidly connected to the upper node of the rotor shaft and azimuthally rotated with 45° with regard to the rotor blade orientation. Only the inplane characteristics are considered, since the original absorber is tuned to suppress rotational 3/rev inplane vibrations. The absorber features two holes of circular shape, each supporting one pin with rolling contact [84, 85]. Likewise, a tuning mass component which features two holes as well is also in rolling contact with the two pins. A general approach to model the dynamical characteristics of the bifilar absorber has been derived for an arbitrary shape of the holes earlier based on curve sliding joints [85]. Another approach to include the bifilar absorber dynamics into simulation is based on a representative one dimensional centrifugal pendulum formulation [36]. In this work an alternative approach is used based on revolute joints. The absorber degrees of freedom are indicated in figure 2. All angles are measured in the x_E-y_E-plane. The two rolling pins of the original absorber are represented by only one rolling pin and additional constraints. The kinematics of the absorber are represented by four revolute joints. The inner joint is located at the center of the inner hole B_E and described by ϕ_i. The outer joint is located at the center of the outer hole D_E and described by ϕ_o. The pin is located at C_E and its rotation is described by ϕ_p. The tuning mass is located at E_E. In case of unequal radii of the inner and outer hole it is necessary to establish a revolute joint at C_E described by χ. However, χ is constrained such that the vector $B_E - A_E$ is always parallel to $E_E - D_E$ by applying the constraint c_1, see equation 4. Mind that χ is noted in negative direction according to figure 2. The original absorber fulfills this constraint since it features two pins which prevent a rotation of the outer tuning mass with respect to the absorber retention arm. The constraint in equation 5 establishes the rolling contact of the pin in the inner hole. The constraint in equation 6 realizes the correct rolling contact of the outer hole.

$$c_1 = \phi_\mathrm{i} + \phi_\mathrm{o} - \chi \tag{4}$$

$$c_2 = \phi_\mathrm{i} \cdot R_\mathrm{i} + \phi_\mathrm{p} \cdot R_\mathrm{p} \tag{5}$$

$$c_3 = \phi_\mathrm{i} \cdot \left(R_\mathrm{i} - R_\mathrm{p}\right) + \phi_\mathrm{o} \cdot \left(R_\mathrm{o} - R_\mathrm{p}\right) \tag{6}$$

The geometry of the bifilar absorber is not available in detail from reviewed literature. Thus the monofilar absorber geometry is used as reference to establish a representation of the bifliar absorber [86]. However, the retention arm length of the monofilar absorber is in reasonable agreement with the simple pendulum representation of the bifilar absorber [36]. The outer hole radius is modified

to tune the absorber frequency towards 3/rev. Note that the outer hole radius is subsequently very close to the inner hole radius. Hence a reasonable approximation is to remove the degree of freedom χ and to set both radii to $R_\mathrm{i} = R_\mathrm{o} = 0.05\mathrm{m}$. The mass properties of the absorber are based on the monofilar absorber as well [86]. Again the tuning mass is in reasonable agreement with the bifilar mass given in ref. [84]. The pin mass properties are taken into account twice because the two pins are only represented by one.

After the assembly of all bodies an angle of $\Phi_{pl} \approx 3^\circ$ would be required to establish geometric integrity. Hence, to establish vertically aligned pitch links in the reference configuration [87], the swash plate geometry is slightly modified, since the exact orientation of the pitch links might be important in future when pitch link loads are investigated. Accordingly, the angle ϕ_pl is slightly reduced to yield $\Phi_{pl} = 0^\circ$. The angle $\phi_\mathrm{sv} = 90^\circ$ is still realized thus the booster position changes slightly in clockwise direction, the forward link is now at $\Psi = 121.217^\circ$ instead of 123.933°, to maintain the same control characteristics.

It is assumed that the one dimensional beam representation of the rotor blades is sufficient, in agreement with ref. [88]. The rotor blade properties can be found following the references in table 5. Structural damping, except for the lag dampers, is neglected in the model. The aerodynamic forces are calculated using 2-D airfoil polars for lift, drag and pitching moment. The polars are observed from literature [17] for both airfoils SC1095 and SC1094R8. The radial twist, chord and airfoil distribution is observed from literature as well and listed in table 5. The inflow velocity is modeled by the Peters-He model (12 modes) which is already integrated into *Dymore* [89]. A representation of the elastic non-rotating control linkage used herein was calculated previously for static displacement using individual servo stiffnesses [87]. In this calculation and for the model herein a rigid swash plate is assumed, although considerable swash plate elasticity seems to be involved [87]. The stiffness for one standalone servo, see ref. [28] is in agreement with the calculated individual stiffnesses, because the control linkage features more flexibility compared to an isolated servo, see table 5. The approach used herein captures unevenly distributed supporting of the static swash plate and the elasticity of the different connections [87].

Rotor Validation

The rotor blade structural non-rotating characteristics are validated using modal data [25]. The eigenvectors from the reference [25] are linearly interpolated at the quarter-chord using the trailing and leading edge deformation. The eigenvalues of all four baseline blades tested without instrumentation are averaged [25]. According to the experimental setup the shaker and the suspension of the blade is modeled by using the properties from literature [25]. Only for this analysis, the number of finite beam elements is increased from 14 to 40. The results are illustrated in figure 3 and in figure 9. The frequencies are in good agreement with the reference, see figure 3. The mode shapes reasonably match the experimental data as well, see figure 9. However, the higher flap modes differ slightly compared to the experimental data.

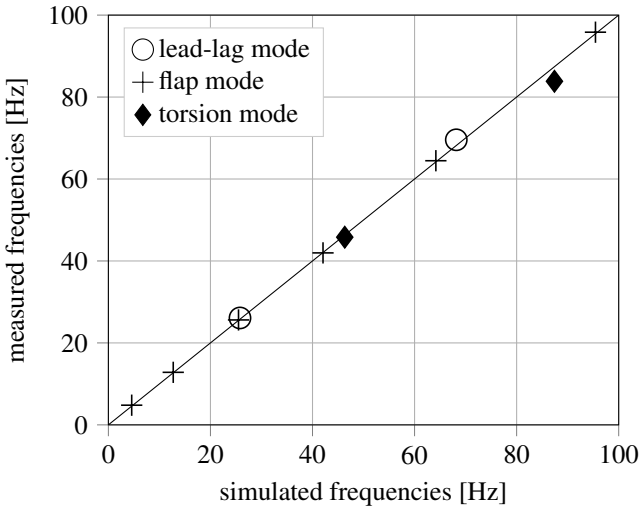

Fig. 3: Comparison of natural UH-60A baseline rotor blade frequencies in the shake test configuration [25].

In the rotating domain the rotor blade structural properties are validated against reference simulations, which have been calculated with *RCAS*, *CAMRAD II* and *Dymore* previously for two different pitch link stiffnesses [90, 91]. For the fan plot analysis herein the shaft elasticity, the servo elasticities and the lag dampers are removed from the rotor assembly and only one blade is considered. In accordance to [90] the pitch link stiffness is kept in one case as nominal, see table 5, and approximately as one third of the nominal stiffness in the other case. The calculated frequencies for both pitch link stiffnesses are in very good agreement with the reference calculated with *RCAS* [90], see figure 4. Moreover, *CAMRAD II* calculations are likewise in very good agreement with the *RCAS* simulation and the calculations of the present work in turn, see ref. [90]. Furthermore, the calculated fan plot results are generally in agreement with another reference calculated with *Dymore* [91], according to figure 4. The calculated result for the reduced pitch link stiffness agrees with reference 2 in trend and magnitude, however, at higher rotational speed the results are slightly overestimated compared to the reference 2 especially for the torsional mode, see figure 4(a). At nominal pitch link stiffness the third flap mode at low rotor rotational speed is overestimated, according to figure 4(b). The other modes are in agreement with reference 2 except for a characteristic which holds for the soft pitch link stiffness as well, namely that the torsional mode frequency is overestimated at rotor speeds higher than the frequency where the second lead-lag mode and the torsional mode are very close. Particularly with regard to reference 1 [90] the effect of pitch link stiffness is assumed to be cap-

tured correctly and the rotor blade properties are assumed to be reasonably represented as well.

For the validation of the aerodynamics in hover, the full scale test campaign in the 80 x 120 ft wind tunnel at NASA Ames is selected as reference [29]. Due to power limitations, hover data is only available up to $\frac{C_T}{\sigma} = 0.07$ [30]. For the hover test, out of groud conditions (HOGE) are assumed, which is in agreement with the measurements [30]. A correction for flight test data was introduced previously to compare free flight data with the wind tunnel hover test results [30]. In this work, the approach is used to expand the validation range by comparison with free flight test data up to a blade loading of $\frac{C_T}{\sigma} = 0.11$. According to literature [30], the main rotor shaft power is calculated from the engine power observed from flight test data [13, 16, 22]. During the flight tests the main rotor thrust was estimated from the gross weight corrected by the consumed fuel mass [22]. Hence, the rotor thrust estimation in free flight is corrected for fuselage download since the simulation is conducted without fuselage blocking effects [30]. From the wind tunnel test campaign, the reference setup with a shaft tilt angle of $\gamma_S = 0^\circ$ is taken into account and a collective sweep from $\frac{C_T}{\sigma} \approx 0.02$ to 0.11 is simulated. In agreement with the test, the bifilar absorbers are not installed in the simulations [29]. Figure 5 shows a good agreement between the simulation and the reference data, however, the wind tunnel power is marginally underestimated.

In forward flight the model is first of all validated based on wind tunnel data from the NASA Ames 80 x 120ft wind tunnel as well [30]. However, only data up to 80knots corresponding to an advancing ratio of $\mu = 0.19$ is available. The considered wind tunnel tests were conducted using a trim towards zero flap motion, which is correspondingly realized in the simulation. The trim controller is already included in *Dymore* which uses the inverse Jacobian matrix of model inputs and trim targets for control settings prediction. Additionally, gains can be selected for each control signal. Only a shaft angle of $\gamma_S = 0^\circ$ is considered in the simulation. Figure 6 shows a good agreement between the wind tunnel data and the simulation at a blade loading of $\frac{C_T}{\sigma} = 0.06$. At higher blade loading the power is significantly overestimated, especially above an advancing ratio of $\mu = 0.1$. According to figure 10(a), the trim targets are well met, since they are within the accuracy of $\pm 0.4^\circ$ which was observed during the test campaign [30]. The flap motion is determined from the blade tip motion. To understand the power discrepancy, figure 6 contains the results which have been calculated with *CHARM* previously [92]. Obviously, this reference exhibits a similar trend. It was demonstrated that taking the wind tunnel walls and the LRTA fuselage into account, the free wake analysis is in agreement with the wind tunnel measurements [92]. Accordingly, the discrepancy was explained by the fact that the rotor aerodynamics are affected by the wind tunnel walls and the fuselage. The explanation is assumed to be valid for the simulation results herein as well, since wind tunnel and fuselage effects are not modeled. Although, still a discrepancy exists between the uncorrected free wake analysis with *CHARM* and the simulation, see figure 6.

$$\alpha_{\text{shaft}} = \Theta_F + \gamma_F \tag{7}$$

$$\gamma_F = -3^\circ \tag{8}$$

Again, to expand the validation range in edgewise flight, free flight test data is used [22]. The trim targets in horizontal flight are observed from literature for the Airloads Program flight test with counter 85 [93]. The counter 85 corresponds to a level flight speed sweep with $\frac{C_T}{\sigma} \approx 0.08$. The air density during the flight test is assumed to be $\rho = 1.13\text{kg}\,\text{m}^{-3}$ [22]. In [22] it is indicated that the airloads flight tests are in agreement with earlier flight test, like 1st year [13], sixth year [14], and 12th year [16] production aircraft tests during the AEFA project. Using the corresponding shaft angles, the wind tunnel test data was previously demonstrated to be in good agreement with the flight test data of counter 85 for a minimum advancing ratio of $\mu = 0.09$ and for a blade loading of $\frac{C_T}{\sigma} = 0.08$ and $\frac{C_T}{\sigma} = 0.09$ [30]. To establish trim conditions in the simulation setup that allow to mimic the rotor in free flight, the shaft angle α_{shaft} according to equation 7 is prescribed in this work for each data point individually. The slope of the shaft tilt angle is depicted in figure 11(d). Additionally the rotor is trimmed towards the shaft bending moments given in ref. [93] and the thrust given in ref. [22]. The rotor power is in agreement with the Airloads Program data according to figure 6. However, at high speed the power is underestimated. The aerodynamic conditions at high speed are not well captured by the steady airfoil aerodynamics used herein. It is emphasized that below an advancing ratio of $\mu = 0.19$ the rotor power at $C_T/\sigma = 0.09$ is not in agreement with the wind tunnel data as discussed earlier. However, at this speed and at a comparable thrust level the simulation is in good agreement with the flight test data. This supports the presumption that wind tunnel and LRTA surfaces are causing the mentioned discrepancy in comparison with wind tunnel data.

The simulated propulsive force which is related to the parasitic drag is in agreement with the Airloads Program reference and a theoretical model introduced in ref. [93] according to figure 11(c). The Airloads Program propulsive force F_x is calculated according to equation 9 with the assumption that the thrust is orthogonal to the TPP. The equation 10 is taken from ref. [93].

$$F_x = -T \cdot \sin\left(\alpha_{\text{TPP,y}}\right) \tag{9}$$

$$\alpha_{\text{TPP,y}} = \alpha_{\text{shaft}} - \beta_{1c} \tag{10}$$

During the simulation the trim settings are properly met as indicated in the figures 10(b) and 11(a). To increase the robustness of the simulation at highest speed ($\mu = 0.368$), the airfoil tables are modified and the angle of attack of $c_{l,max}$ is increased about 4° using linear extrapolation, to provide a strictly monotone lift curve slope at high angles of attack. Otherwise, the solution diverges in unsteady

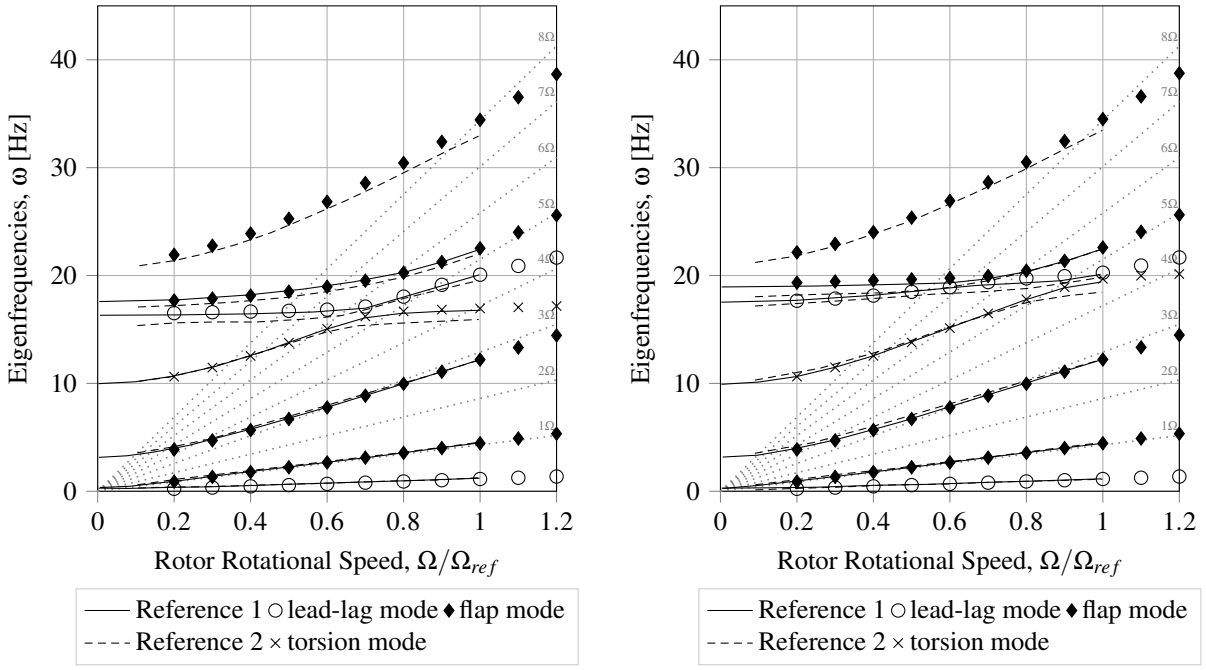

(a) Fan plot calculated with soft pitch link stiffness.

(b) Fan plot calculated with nominal pitch link stiffness.

Fig. 4: Comparison of calculated UH-60A baseline rotor blade frequencies in the rotating domain and Reference 1 [90], Reference 2 [91].

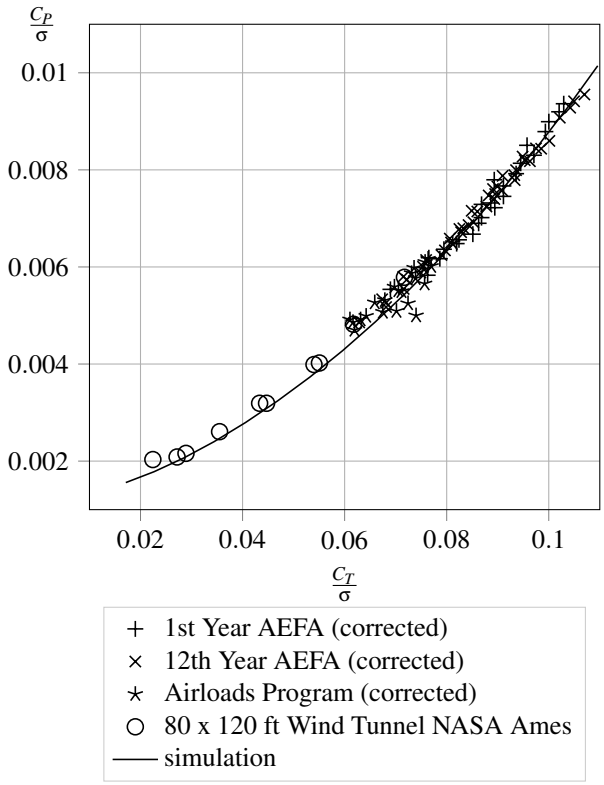

Fig. 5: UH-60A hover performance calculated in wind tunnel configuration in out of ground effect conditions and compared to literature [22,30].

flight conditions like horizontal speed up, once $c_{l,max}$ is passed, which is identified to result from the control characteristic inversion. In the steady flight conditions discussed in this work, the rotor is not operated in the modified lift range. In figure 11(e) the coning and lead-lag motion is depicted in comparison with the flight test data. The simulated blade motion is evaluated at the corresponding hinge. The lead-lag motion is in good agreement with the test data, according to figure 11(e). The coning shows a significant offset. This characteristic was previously observed using *CAMRAD II* simulations and it was shown that the simulation results are in agreement with the theoretical coning angle [93]. This holds for the simulation herein as well.

The lateral flap motion is slightly overestimated above $\mu \approx 0.23$ and the longitudinal flap motion is overestimated up to $\mu \approx 0.3$ and afterwards underestimated, see figure 11(f). In general, the flap motion represents the experimental trends correctly. In the past an unresolved phase offset in the experimental flap motion of $\approx 45°$ was mentioned by different authors [27, 90, 94]. After the PD/B azimuth correction the offset is reduced by 14° to $\approx 31°$ [27]. In these cases rotor simulations have been conducted with prescribed airloads from experiments [90, 94]. In this work airloads are computed and thus, the offset is not visible in the flap motion because flapping is reinforced by the trim target shaft moments. However, the offset of $\approx 31°$ is visible by comparing the simulated and the experimental feathering motion. If the feathering motion is corrected about 31° phase offset the simulated lateral pitch motion is in agreement with test data, see figure 11(b). Note that in the related reference [93] the pilot control angles are given. Hence, pilot cyclic inputs are converted into blade root pitch motion. The longitudinal pitch agrees with the experi-

mental data at low speed. At higher speeds the longitudinal pitch is significantly overestimated. This disagreement was also observed in previous calculations using *CAMRAD II*, however lateral cyclic corresponding to longitudinal pitch was significantly underestimated [93].

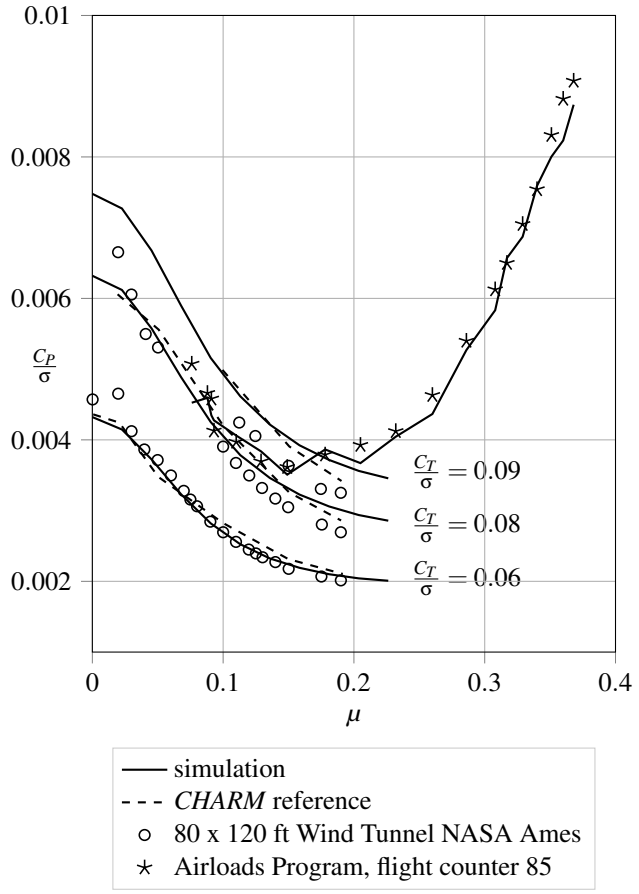

Fig. 6: UH-60A performance in trimmed horizontal edgewise flight. Three different blade loading conditions in a wind tunnel setup and a velocity sweep according to Airloads flight test counter 85 calculated and compared to literature [22,30,93].

Fuselage Model

Both rigid and elastic motion of the fuselage are assumed to remain small enough for linear approximation of governing equations of motion. Hence rigid and elastic motion is represented using modal coordinates. This approach has been used in the past for rotor fuselage coupling as well [36, 37, 44, 84, 95, 96]. Besides these approaches often so-called stick models are used in previous work to represent the elasticity of the fuselage with beams [46,49,78,79,85,97]. However, stick models do not represent the fuselage dynamics appropriately [46] and are not used in this work.

From literature two independent models are selected which are herein referred to as *DAMVIBS* [33] and *HUBNODE* [37] configuration. Both models have been used in the past for rotor-fuselage coupled analysis [78, 84]. For the NASA/AEFA configuration sufficient data could not be observed [34]. The *HUBNODE* configuration exclusively approximates structural UH-60A main rotor hub node dynamics using nine modes incorporating three translational and three rotational degrees of freedom, see table 6. The frequencies and the damping rations are given in the references explicitly [36, 37]. The modal masses given in $lb - s^2/in$ are scaled to kg by $g \cdot 0.453592/0.0254$. The second factor scales pounds to kg and the third converts 1/in to 1/m. Note that modal data presented in this work is given with modal masses strictly scaled towards unity. Hence, the mode shapes are scaled with $\frac{1}{\sqrt{\tilde{m}_k}}$, see equation 18.

Reference rigid body properties can be observed from literature [17, 20, 35, 47, 98]. From these references, properties are selected which match the helicopter configuration of the Airloads program counter 85 the closest. During the flight test the mean weight coefficient is $C_W/\sigma \approx 0.079$. From ref. [98] a configuration is selected with a weight coefficient of $C_W/\sigma = 0.0762$, which is 3.5% mismatch. However, data more close is not available from reviewed literature. According to ref. [98] the fuselage is symmetric. The selected properties agree reasonably with the design properties according to ref. [15, 17, 99]. Furthermore, the COG location of this configuration is very close to the COG location of the MTRA configuration [48]. The rigid body properties of the fuselage are summarized in table 1.

weight	7438.9 kg		
I_{xx}	7631.95 kg m^2	$x_{aeroref}$	8.776 m
I_{yy}	54233.08 kg m^2	$z_{aeroref}$	5.944 m
I_{zz}	50436.73 kg m^2	$x_{hs,ref}$	17.790 m
I_{xz}	2264.23 kg m^2	$z_{hs,ref}$	6.198 m
x_{CG}	9.154 m	$x_{vs,ref}$	17.653 m
z_{CG}	6.279 m	$z_{vs,ref}$	6.934 m
$x_{mr,hub}$	8.666 m	$x_{tr,hub}$	18.593 m
$z_{mr,hub}$	8.001 m	$z_{tr,hub}$	8.247 m

Table 1: Reference properties of the rigid UH-60A fuselage [98]. All points given in the table are assumed to be located in the fuselage plane of symmetry and given in the construction frame. Coordinate system orientation: x points rearward, z points upward.

A modal approximation of the rigid fuselage motion is computed from fuselage inertia and mass given in table 1 according to the following logic. Linearization of Newton-Euler equation for spatial rigid body motion for an arbitrary point Q of a rigid body yields [100]:

$$\overbrace{\begin{pmatrix} m\boldsymbol{I} & m\tilde{\boldsymbol{r}}_{CQ} \\ -m\tilde{\boldsymbol{r}}_{CQ} & \boldsymbol{\Theta}_Q \end{pmatrix}}^{=:M_Q} \overbrace{\begin{pmatrix} \ddot{\boldsymbol{u}}_Q \\ \dot{\tilde{\boldsymbol{\omega}}} \end{pmatrix}}^{=:\ddot{\boldsymbol{x}}_Q} = \overbrace{\begin{pmatrix} \boldsymbol{F}_Q \\ \boldsymbol{M}_Q \end{pmatrix}}^{=:F_Q} \tag{11}$$

where $\tilde{\boldsymbol{r}}_{CQ}$ is the skew matrix representation of the corresponding vector $\boldsymbol{r}_{CQ}$ and C is located at the body center of

gravity. Now equation 11 is simplified by choosing Q as the center of gravity, hence:

$$\overbrace{\begin{pmatrix} m\boldsymbol{I} & \boldsymbol{0} \\ \boldsymbol{0} & \boldsymbol{\Theta}_C \end{pmatrix}}^{=:M_C} \overbrace{\begin{pmatrix} \ddot{\boldsymbol{u}}_C \\ \ddot{\boldsymbol{\theta}} \end{pmatrix}}^{=:\ddot{\boldsymbol{x}}_C} = \overbrace{\begin{pmatrix} \boldsymbol{F}_C \\ \boldsymbol{M}_C \end{pmatrix}}^{=:F_C} \tag{12}$$

In table 1 the inertia with respect to the center of gravity $\boldsymbol{\Theta}_C$ are given. To convert the states and the loads between the two reference points Q and C the equations 13 and 14 can be used.

$$\ddot{\boldsymbol{x}}_Q = \kappa_{QC} \ddot{\boldsymbol{x}}_C \tag{13}$$

$$F_C = \kappa_{QC}^T F_Q \tag{14}$$

$$\text{where: } \kappa_{QC} = \begin{pmatrix} \boldsymbol{I} & -\tilde{\boldsymbol{r}}_{CQ} \\ \boldsymbol{0} & \boldsymbol{I} \end{pmatrix} \tag{15}$$

$$\kappa_{QC}^{-1} = \begin{pmatrix} \boldsymbol{I} & \tilde{\boldsymbol{r}}_{CQ} \\ \boldsymbol{0} & \boldsymbol{I} \end{pmatrix} \tag{16}$$

It holds $M_Q = \kappa_{QC}^{-T} M_C \kappa_{QC}^{-1}$. If M_C is already a diagonal matrix, the state vector $\ddot{\boldsymbol{x}}_C$ can be interpreted as the generalized coordinates of the rigid fuselage with the corresponding modal matrix $\tilde{\boldsymbol{r}}_{CQ}$. In general, $\boldsymbol{\Theta}_C$ is not diagonal, hence the modal matrix ϕ_C is calculated from matrix M_C to find the inertia principle axes and to find decoupled states and the corresponding diagonal mass matrix M. Hence, for a mode k the mass scaled rigid body mode shape for each point Q_i can be observed from $(\kappa_{Q_iC} \cdot \phi_{C,k}) / \sqrt{\tilde{m}_k}$. And $\tilde{m}_k$ are the diagonal elements of matrix M.

The rigid body modes at the main rotor hub according to the properties in table 1 are given in table 2. The fuselage configuration for the *HUBNODE* mode shapes in table 6 is not evident from literature [36, 37, 84]. However, the values of the two rigid fuselage modal representations are comparable, see table 2 and table 6, except for the different signs of mode 4 and 6 and two additional non-zero entries in the calculated model which result from the moment of deviation I_{xz} given in table 1.

In figure 12 the calculated transfer functions of the *HUBNODE* model, using the elastic modes given in table 6, are compared to shake test data and reference simulation results [37]. In contrast to the figures depicted in literature [37] the absolute values of the amplitude are depicted. The results are in good agreement with the reference data. Especially the magnitudes of the most dominant components are well captured. Thus, the model is assumed to be correctly implemented. Mind that for the second transfer function no test data is available between 14.9 Hz and 15.7 Hz.

The herein selected nodes of the *DAMVIBS* model and its modal data are listed in table 7. To realize main rotor coupling the nodes 65 and 66 are included as well as the nodes 23, 30, 31 to capture the motion of the non-rotating swash plate support and to account for fuselage coupled control inputs later, according to the reference node numbers [33]. Node 72 is included for tail rotor fuselage coupling. Additional nodes are selected for future tail shake analysis using the nodes 55, 57, 59 (vertical tail), 60, 62, 64 (horizontal tail) and for assessment of cabin vibrations using the nodes 07, 09, 10 (cockpit), 33, 36 (payload bay). Note that these nodes are selected since required data is not available for each node of interest [33].

mode	f [Hz]	D [%]	x y z	r_x r_y r_z
			0.0115943	0
1	0.0	0.0	0	0
			0	0
			0	0
2	0.0	0.0	0.0115943	0
			0	0
			0	0
3	0.0	0.0	0	0
			0.0115943	0
			0	0.0115214
4	0.0	0.0	-0.0195432	0
			0	-0.0006077
			0.0073944	0
5	0.0	0.0	0	0.0042941
			0.0020955	0
			0	0.0002343
6	0.0	0.0	-0.0025708	0
			0	0.0044413

Table 2: Modal main rotor hub properties of the rigid UH-60A fuselage calculated from properties given in table 1.

During the shake tests test *DAMVIBS* fuselage was supported by suspension systems. In the shake test results, a coupling between the first elastic mode and the suspension system was discovered [34]. But in this work, the suspension system is neglected. In the reference data occasionally a significant frequency of ≈ 4.8Hz is included in the transfer functions, which is neglected in this work as well since this mode was mentioned or identified neither in the reference itself nor in other references [33]. The mode is predominantly visible at the tail rotor gear box node and the tail rotor hub node in the lateral and vertical response to an excitation in lateral direction at the main rotor hub. In addition two modes of the *DAMVIBS* configuration which have been experimentally identified (Stabilator rigid body II & Stabilator Yaw) are not included in the model described herein, since relevant data is not available. Beyond that, additional modes were identified in the finite element analysis which are neither included in the model herein. Note that for the NASA/AEFA configuration [34] and the MRTA configuration the modal properties from finite element analysis change significantly due to flight test instrumentation and additional equipment [26, 48].

In figure 7 the frequencies of the fuselage model and the graphically estimated frequencies from transfer functions are compared to the *DAMVIBS* model frequencies given in ref. [33]. Apparently, the frequencies of both models do not

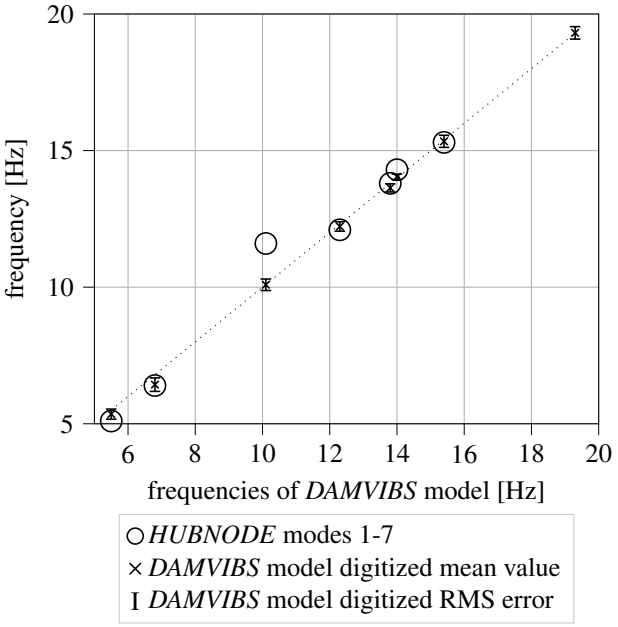

Fig. 7: UH-60A fuselage elastic frequencies. Graphically determined frequencies based on transfer function [33] and frequencies given in literature [33, 36] are compared.

match. The first two frequencies of the *HUBNODE* configuration are lower compared to the *DAMVIBS* model and the frequency of mode 3 is significantly higher. The digitized data reveals that the corresponding frequencies do match with the frequencies of the *DAMVIBS* model on average except for the second fuselage mode. Figure 7 indicates that the graphically observed frequency of the second mode matches instead with the corresponding frequency of the *HUBNODE* configuration [36, 37]. Consequently, the frequency of the second *DAMVIBS* mode is adjusted 6.4Hz. In figure 7 a root mean square error of the digitized frequencies is visible of $\sigma \approx 0.19$Hz on average. This is most likely due to the manual selection of the frequencies. The damping ratios of the two models *HUBNODE* and *DAMVIBS* are in agreement, except for the first, second and fourth mode where the damping ratios of the *DAMVIBS* model are much lower, see tables 6 and 7. It is anticipated that the damping ratios from the *HUBNODE* model are blanketly selected as 0.025 which is a good approximation of the higher modes according to *DAMVIBS* model.

For the *DAMVIBS* configuration modal masses and mode shapes are not given explicitly in literature, however, the transfer functions are given that include all necessary information [33]. To establish a modal representation a mismatch measure η is used, see equation 19. η takes all selected transfer functions into account and calculates the mismatch between the simulation and the reference. The reference tests have been conducted by applying forces in longitudinal, lateral and vertical direction at the hub exclusively [33]. Yet, for a certain degree of freedom measurements are in general not available for all forcing directions. The transfer behavior in magnitude from DOF with index i to DOF with index j at the excitation frequency ω_l is written as H_{ijl}, see equation 17. H_{ijl} is observed from literature for a discrete number of frequencies. For the optimization of mode shapes, the frequencies ω_l are selected to match the harmonics denoted by index k. Thus the refined calculation of the mode shapes is designed towards minimizing the error at the transfer function peaks. Since the modal masses $\tilde{m}_k$ are all scaled to unity and both the frequencies ω_k and the damping rations D_k are known from literature [33], the input-output magnitude relationship is only depending on the mass scaled eigenvalues $\tilde{\phi}_{ik}$ and the phases do not have to be considered in η. Since H_{ijl} involves in general two eigenvector entries of all modes except for the collocated case, where only one entry of each eigenvector is involved, the elements of the eigenvectors can not be determined individually.

$$H_{ijl} = \left\| \sum_k \frac{\tilde{\phi}_{ik} \cdot \tilde{\phi}_{jk}}{\omega_k^2 - \omega_l^2 + \mathrm{i}2D_k\omega_k} \right\|_2 \tag{17}$$

$$\text{where } \tilde{\phi}_{ik} = \phi_{ik}/\sqrt{\tilde{m}_k} \tag{18}$$

$$\eta^2 = \overline{\left(H_{ijl} - H_{ijl,ref}\right)^2} / \overline{H_{ijl,ref}^2} \tag{19}$$

The determination of the mode shapes from literature is done in four steps. This approach gives the best results compared to other tested approaches. First the mode shapes are estimated graphically from figures in literature [33] and appropriate modal masses are selected manually. Second, these values serve as an initial solution for a subsequent minimization of η, see equation 19. Rigid body modes are neglected during the minimization. Third, after η is minimized successfully, all eigenvectors are compared to the depicted mode shapes again. In some cases, it is necessary to set eigenvector values to zero after minimization manually. Last, the transfer functions are rechecked if zeroing elements cause significant discrepancies.

The transfer characteristics are shown for the main rotor hub node since it is not possible to illustrate all 102 considered transfer functions. The transfer functions at the main rotor head are in good agreement with the reference test data, see figure 13. Note that the frequencies of the spikes do not match exactly, due to inaccuracies in the digitalization and disagreements in the frequencies and transfer functions in the reference data itself [33]. The transfer functions are calculated with and without the rigid body modes included. Since the difference is small, the determination of the elastic mode shapes without taking the rigid mode shapes into account is confirmed to be acceptable. In figure 13(e) the spikes at > 20Hz are not captured by the model herein since the frequencies are beyond the considered range. Figure 13(b) indicates an inconsistency in the reference data since the transfer characteristics from longitudinal direction to the lateral direction and vice versa disagree especially at frequencies higher than ≈ 12Hz. The result of the minimization of η is consistently in between. In the other depicted non-collocated cases the data agrees

much better. All transfer functions which are not depicted in this work are comparable in magnitude with the ones exemplarily shown, except for lateral direction pilot floor response to excitation in longitudinal direction at the main rotor hub (one decade overestimated), and the lateral response of the tail rotor hub to excitation in longitudinal direction at the main rotor hub (nearly one decade underestimated). The first transfer function is of low magnitude compared to the others and assumed not to be adequately represented in the cost function η. The second transfer function only disagrees significantly at the modes 2-5.

The models are compared based on the main rotor hub node. For comparison the corresponding transfer functions of the *DAMVIBS* model are as well depicted in figure 12. Obviously, there is no noticeable agreement between both models. The magnitudes of the *HUBNODE* model are significantly higher at a frequency of 14Hz to 15Hz and lower at low frequencies compared to *DAMVIBS* model. In table 3 the mode shapes are compared by means of MSF and MAC criterion. The criteria are applied to previously matched modes since the number of included DOF (3) is much lower than the number of considered modes (8 and 9) which results in rank deficiencies of the modal matrix. Consequently, the criteria would indicate many matches among the modes, because too little information is considered for each mode. However, the modes are selected corresponding to the frequencies and show reasonable agreement in terms of MSF and MAC at low frequencies, see table 3. Whereas there is no agreement in MAC at the fifth mode and higher. For MSF values lower than one, a smaller transfer function value of the *DAMVIBS* model would be expected. However, figure 12 indicates the opposite. This can be explained by the fact that the damping ratios of the *DAMVIBS* model are lower compared to the *HUBNODE* model. The agreement of MAC and MSF for the third modes is surprising since the corresponding frequencies differ significantly, see figure 7.

HUBNODE	*DAMVIBS*	MSF	MAC
mode 1	mode 1	0.7054	0.9895
mode 2	mode 2	0.8185	0.9868
mode 3	mode 3	0.8703	0.7452
mode 4	mode 4	1.1875	0.7637
mode 5	mode 5	0.4116	0.1333
mode 6	mode 6	0.0093	0.0001
mode 7	mode 7	0.0545	0.0079
mode 8	mode 8	0.4566	0.4264
mode 9	mode 8	0.7332	0.0545

Table 3: MAC and MSF for selected mode combinations of model *HUBNODE* and *DAMVIBS* configuration. Sign of MSF neglected.

Coupled Rotor-Fuselage Analysis

The coupled rotor fuselage analysis includes the models described in the first two sections, namely the rotor model and the fuselage model. To represent the fuselage, the *HUBNODE* configuration is selected to investigate the influence of rotational degrees of freedom which are not available for the *DAMVIBS* configuration. Since the node of this model is located at the main rotor hub, the rotor shaft elasticity is assumed to be already represented by the elastic fuselage model, hence a rigid rotor mast with the same geometry as described earlier is used and combined with the modal fuselage representation. This approach has already been used in the past by other researchers [101].

In context of the Airloads Program flight counter 85 the calculated hub accelerations are compared to test data [48]. Discrepancies are expected since the counter 85 consists of flight states where significant blade vortex interaction (counter 8513) and helicopter high speed phenomena (counter 8534) occur, which are expected not to be adequately resolved by the used aerodynamic representation. The counter 8513 and the counter 8534 have often been referenced in the past due to the highly complex phenomena involved [23, 24, 70, 74, 87, 90, 102–109]. During the coupled analysis the trim settings are properly met. The hub accelerations are calculated over 20 rotor revolutions. Forces and displacements are exchanged each time step ($\Delta t = 0.001$s). At the main rotor hub, rotor torque is not imposed on the fuselage model since the shaft bearing transfers no moment in shaft direction between rotor and fuselage. No vibratory displacement in shaft direction is imposed on the rotor consistently.

In the simulation no logic is integrated to trim and stabilize the rigid body fuselage motion. Hence, the RBM are neglected in the coupled analysis. In figure 14 the results of three different simulation setups are depicted. The coupled simulation with all DOF involved underestimates the mean half peak-to-peak accelerations in both in-plane and out-of-plane direction significantly compared to flight test data [48], see figures 14(a) and 14(b). The 4/rev out-of-plane and 3/rev in-plane harmonics agree with test data at low speed and are overestimated at higher advancing ratios, see figures 14(c) and 14(e). 8/rev out-of-plane as well as the 5/rev in-plane harmonics are in agreement with the test experimental reference, see figures 14(d) and 14(f). If the rotatory DOF are neglected in the analysis, the in-plane 5/rev harmonics, the mean half peak-to-peak accelerations and the 4/rev out-of-plane harmonics decrease. If the rotor is calculated with a hub fixed support, the fuselage hub accelerations are significantly higher compared to the simulation with displacement feedback, except for the out-of-plane 8/rev harmonics. Note that previous simulations using the *HUBNODE* configuration for coupled analysis [84] the 3/rev in-plane accelerations do agree with the reference test data [48]. An explanation for the disagreement of 3/rev in-plane harmonics is that the bifilar absorbers are not activated in this work which however reduce the vibrations in

flight test and in the reference simulation [48, 84].

Conclusion

The rotor model described herein is successfully validated against available experimental data. The rotor structural representation is sufficient for future analysis. The *DAMVIBS* fuselage model is established based on available experimental data as well. The two different modal representations of the main rotor hub node agree at low but not at higher frequencies. All in all, the eigenvectors are assumed to be correctly reconstructed from the available reference data, although the comparison at only one node is not sufficient to claim the correctness of all eigenvector entries. It should be possible to setup the model described herein from the data and references given in this work. The processed and presented fuselage data from literature allows to directly feed simulation programs and to use modal space fuselage representation for efficient rotor-fuselage coupled analysis.

Two particular shortcomings in this work in comparison to experimental results are the prediction of the rotor blade feathering motion and the hub accelerations. At higher advancing ratios the feathering motion does not agree with the experimental data. An inconsistency between the flap and feathering motion in comparison with the Airloads flight test data is discovered. This could be related to obscure azimuth reference and an azimuth offset which has already been mentioned by other researchers [90, 94].

Beside the magnitude, the accelerations do not agree in their characteristic over different horizontal flight speeds [110]. The half peak-to-peak mean accelerations are significantly underestimated in contrast to the individual harmonics. In particular, the high accelerations at $\mu \approx 0.1$ and $\mu > 0.3$ are not captured [48]. This trend correlates with the shaft pitching moment used in this work as trim target, which indicates empennage interference effects [93]. For better representation of the mean half peak-to-peak in-plane and out-of-plane accelerations the rigid body modes as well as interactional aerodynamics should be included into the simulation [93, 110]. This requires to modify the trim strategy. Although the results calculated with fixed rotor support agree better in magnitude with test data, however not in trend, the physics are not better represented compared to an elastic rotor support. To improve in-plane 3/rev acceleration the bifilar absorbers should be integrated into the coupled rotor fuselage simulation. The rotational degrees of freedom have an effect on the translational hub accelerations. In this work the control linkage connections between the rotor system and the fuselage are neglected, since the selected modal representation only consists of the main rotor hub node. In general, it is important to take all connections between the rotor system and the fuselage into consideration [38, 111]. Besides the rotor shaft this includes the control linkage as well. On the one hand structural vibrations can be transmitted via the control linkage system and fuselage motion can introduce feedback control inputs which may lead to significant loads on the other hand [111].

Future Works

The validation cases available from reviewed literature are limited, hence additional detailed data is necessary. A refinement for structural loads prediction could be the integration of the drive train and gearboxes [17, 20, 101, 112]. The control linkage connection at the fuselage could be modeled in addition to the hub connection to cover feedback control inputs introduced by fuselage motion [38, 111]. The coupled rotor-fuselage simulation could be further improved using Herting's mode synthesis approach [46, 113]. To better represent blade sectional loads and vibratory hub loads, refined and unsteady aerodynamic representations such as Leishman-Beddoes, Free-Wake or even CFD are required [38, 40, 63, 67, 101, 106, 114]. The tail rotor and aerodynamic rotor-fuselage, rotor-empennage and rotor-rotor interactions could be considered in future since they affect the vibratory content significantly [40, 93]. Hence, trimmed free-flight scenarios could be simulated since trim attitude and helicopter motion affect vibrations. In this context the stability augmentation system, auto-pilot and rigging characteristics can be added for better flight dynamics representation [115–117]. Gain scheduling and analytical estimation of the Jacobian matrices [118] or advanced controller architectures [119] could be used to improve the trim strategy. For future optimization and Monte Carlo simulation tasks of trimmed flight states the trim solver could be replaced by periodic shooting or harmonic balance to solve directly for periodic solutions [120].

Acknowledgment

This work is supported by the German Federal Ministry for Economic Affairs and Energy through the German Aviation Research Programs LuFo V-2 & LuFo V-3 and the Austrian Research Promotion Agency through the Austrian Research Program TAKE OFF in the projects VARISPEED and CORINNE. The authors thank Markus Rinker, M.Sc. for his expertise and for indicating key references for this work as well as Georg Tietze, B.Sc. for the contribution during his term project.

Supported by:

on the basis of a decision
by the German Bundestag

Austrian
Research Promotion Agency

References

[1]Cesnik, Mok, Parikh, and Shin, "Optimization Design Framework for Integrally Twisted Helicopter Blades," *AIAA Conference*, 2004.

[2]Mok, *Design Optimization for Active Twist Rotor Blades*, Ph.D. thesis, University of Michigan, 2010.

[3]Cesnik, Mok, Morillo, and Parikh, "Design Optimization of Active Twist Rotor Blades," *European Rotorcraft Forum*, 2005.

[4]Wang, Diskin, Biedron, Nielson, and Bauchau, "Sensitivity Analysis of Multidisciplinary Rotorcraft Simulations," *SciTech*, 2017.

[5]Gunduz, *Software Integration for Automated Stability Analysis and Design Optimization of a Bearingless Rotor Blade*, Ph.D. thesis, Georgia Institute of Technology, 2010.

[6]Ku, Volovoi, and Hodges, "Multilevel-Multiphase Optimization of Composite Rotor Blade with Surrogate Model," *AIAA Conference*, 2007.

[7]Li, *Structural Design of Composite Rotor Blades with Consideration of Manufacturability, Durability and Manufacturing Uncertainties*, Ph.D. thesis, Georgia Institute of Technology, 2008.

[8]Sidle, Sridharan, Chopra, Feshler, and Kull, "Investigation of Engine-Airframe Vibration Due to Main Rotor Hub Loads Using a Substructuring Framework," *American Helicopter Society Annual Forum*, 2017.

[9]"Utility Tactical Transport Aircraft System (UTTAS)," Tech. rep., US Army, US General Accounting Office, 1974.

[10]Leoni, *Black Hawk The Story of a World Class Helicopter*, AIAA, 2007.

[11]Wissink, Staruk, Tran, Roget, Jayaraman, Sitaraman, and Lakshminarayan, "Overview of New Capabilities in Helios Version 9.0," *AIAA SciTech*, 2019.

[12]McColl, Bauchau, Sonneville, deMontfort, Harper, McGinty, and Bazilevs, "The Load Confluence Algorithm Applied to a Combined Rotor-Fuselage Loads Model with Extended Application to Structural Fatigue Life Tracking," *VFS Annual Forum*, 2019.

[13]Nagata, Skinner, and Buckanin, "Airworthiness and Flight Characteristics Evaluation UH-60A (Black Hawk) Helicopter," Tech. rep., USAAEFA, 1981.

[14]Buckanin, Skinner, Herbst, and Cassil, "Airworthiness And Flight Characteristics Test of a Sixth Year Production UH-60A," Tech. rep., US Army Report, 1985.

[15]Buckanin, Gould, and Young, "Rotor System Evaluation Phase I," Tech. rep., USAAEFA, 1988.

[16]Nagata, Piotrowski, and Young, "Baseline Performance Verification of the 12th Year Production UH-60A Black Hawk Helicopter," Tech. rep., AEFA, 1989.

[17]Howlett, "UH-60A Black Hawk Engineering Simulation Program - Volume I - Mathematical Model," Tech. rep., NASA Contractor Report, 1981.

[18]Howlett, "UH-60A Black Hawk Engineering Simulation Program - Volume II-Background Report," Tech. rep., NASA Ames, 1988.

[19]Kaplita, "UH-60 Black Hawk Engineering Simulation Model Validation and Proposed Modifications," Tech. rep., NASA, 1985.

[20]Abbott, Olivier, Benson, and Williams, "Validation Flight Test of UH-60A for Rotorcraft Systems Integration Simulator (RSIS)," Tech. rep., US Army, 1982.

[21]Watts and Cross, "The NASA Modern Technology Rotors Program," *AIAA*, 1986.

[22]Bousman and Kufeld, "UH-60A Airloads Catalog," Tech. rep., NASA, 2005.

[23]Kufeld, Balough, Cross, Studebaker, Jennison, and Bousman, "Flight Testing the UH-60A Airloads Aircraft," *AHS Forum*, 1994.

[24]Kufeld and Bousman, "UH-60A Helicopter Rotor Airloads Measured in Flight," *The Aeronautical Journal of the Royal Aeronautical Society*, 1997.

[25]Hamade and Kufeld, "Modal Analysis of UH-60A Instrumented Rotor Blades," Tech. rep., NASA Technical Memorandum, 1990.

[26]Idosor and Seible, "Nastran Modeling of Flight Test Components for UH-60A Airloads Program Test Configuration," Tech. rep., NASA Contractor Report, 1993.

[27]Kufeld and Bousman, "UH-60A Airloads Program Azimuth Reference Correction Technical Note," *Journal of the American Helicopter Society*, 2005.

[28]Davis, "Predesign Study For a Modern 4-Bladeed Rotor for the RSRA," Tech. rep., NASA Contractor Report, 1981.

[29]Norman, Shinoda, Kitaplioglu, Jacklin, and Sheikman, "Low-Speed Wind Tunnel Investigation of a Full-Scale UH-60 Rotor System," *AHS Forum*, 2002.

[30]Shinoda, Yeo, and Norman, "Rotor Performance of a UH-60 Rotor System in the NASA Ames 80- by 120-Foot Wind Tunnel," *AHS Forum*, 2002.

[31]Norman, Shinoda, Peterson, and Datta, "Full-Scale Wind Tunnel Test of the UH-60A Airloads Rotor," *AHS Forum*, 2011.

[32]van Aken, Shinoda, and Haddad, "Development of a Calibration Rig for a Large Mulit-Component Rotor Balance," *International Instrumentation Symposium*, 2000.

[33]Howland, Durno, and Twomey, "Ground Shake Test of the UH-60A Helicopter Airframe and Comparison with Nastran Finite Element Model Predictions," Tech. rep., NASA Contractor Report, 1990.

[34]Idosor and Seible, "Comparison of Nastran Analysis with Ground Vibration Results of UH-60A NASA-AEFA Test Configuration," Tech. rep., NASA Contractor Report, 1990.

[35]Dinyovszky and Twomey, "Plan Formulate and Discuss a Nastran Finite Element Model of the UH-60 Helicopter Airframe," Tech. rep., NASA Contractor Report, 1990.

[36]Cassarino and Mouzakis, "Bifilar Analysis Users Manual - Volume II," Tech. rep., NASA, 1980.

[37]Miao and Mouzakis, "Bifilar Analysis Study - Volume I," Tech. rep., NASA Contractor Report, 1980.

[38]Johnston and Cassarino, "Aeroelastic Rotor Stabiliy Analysis," Tech. rep., Final Report, 1976.

[39]Hohenemser, "The Role of Rotor Impedance in the Vibration Analysis of Rotorcraft," Tech. rep., Washington University, 1978.

[40]Sopher, Studwell, Cassarino, and Kottapalli, "Coupled Rotor-Airframe Vibration Analysis," Tech. rep., NASA Contractor Report, 1982.

[41]Sutton and Bennett, "Aeroelastic-aerodynamic optimization of high speed helicopter-compound rotor," *NASA*, 1984.

[42]Adelman and Mantay, "Integrated Multidisciplinary Optimization of Rotorcraft A Plan for Development," Tech. rep., NASA Technical Memorandum, 1989.

[43]O'Brien and Smith, "Analysis of Rotor-Fuselage Interactions Using Various Rotor Models," *AIAA Meeting*, 2005.

[44]Chiu and Friedmann, "A Coupled Helicopter Rotor-Fuselage Aeroelastic Response Model for ACSR," *AIAA Conference*, 1995.

[45]Sidle, Sridharan, and Chopra, "Coupled Vibration Prediction of Rotor-Airframe-Drivetrain-Engine Dynamics," *AHS Forum*, 2018.

[46]Bauchau, Rodriguez, and Chen, "Coupled Rotor-Fuselage Analysis with Finite Motions Using Component Mode Synthesis," *Journal of the American Helicopter Society*, 2004.

[47]Fries, "Helicopter Forced Response Vibration Analysis Method RTVIB20," Tech. rep., U.S. Army Research Laboratory, 1993.

[48]Studebaker, "A Survey of Hub Vibration for the UH-60A Airloads Research Aircraft," *American Helicopter Society Aeromechanics Specialists Conference*, 1994.

[49]Bauchau, Bottasso, and Nikishkov, "Modeling Rotorcraft Dynamics with Finite Element Multibody Procedures," *Mathematical and Computer Modelling*, 2001.

[50]Heo, *Parallel Computation Algorithms for Multibody Dynamics Simulations*, Ph.D. thesis, Georgia Institute of Technology, 2017.

[51]Lee and Hodges, "Multi-Flexible-Body Analysis for Application to Wind Turbine Control Design," Tech. rep., NREL Report, 2003.

[52]Skjoldan and Bauchau, "Determination of Modal Parameters in Complex Nonlinear Systems," *Journal of Computational and Nonlinear Dynamics*, 2010.

[53]Lynch, *Advanced CFD Methods for Wind Turbine Analysis*, Ph.D. thesis, Georgia Institute of Technology, 2011.

[54]Shin, Cesnik, and Hall, "Design and Simulation of Integral Twist Control for Helicopter Vibration Reduction," *International Journal of Control, Automation and Systems*, 2007.

[55]Shen, Masarati, Roget, Piatak, Singleton, and Nixon, "Modeling a Sitff-Inplane Tiltrotor Using Two Multibody Analyses A Validation Study," *AHS Forum*, 2008.

[56]Park, Jung, Park, and Yu, "Correlation study of a rotor in descending flight using DYMORE with a freewake model," *Journal of Mechanical Science and Technology*, 2010.

[57]Ding and Shen, "Helicopter Rotor Infield Tracking with a Trailing-Edge Flap and Adaptive Closed-Loop Regulator," *AHS Forum*, 2018.

[58]Roget, "Simulation of Active Twist and Active Flap Control on a Model-Scale Helicopter Rotor," *Applied Aeromechanics Conference*, 2006.

[59]Bain, Sankar, Prasad, Bauchau, Peters, and He, "Computational Modeling of Variable-Droop Leading Edge in Forward Flight," *Journal of Aircraft*, 2009.

[60]Agarwal, *Aeromechanical Stability Augmentation Using Semi-Active Friction-Based Lead-Lag Damper*, Ph.D. thesis, Georgia Institute of Technology, 2005.

[61]McColl, Palmer, Chierichetti, Bauchau, and Ruzzene, "Comprehensive UH-60 Loads Model Validation," *AHS Forum*, 2010.

[62]Bauchau and Ahmad, "Advanced CFD and CSD Methods for Multidisciplinary Applications in Rotorcraft Problems," *AIAA Symposium on Multidisciplinary Analysis and Optimization*, 1996.

[63]Sitaraman, *CFD Based Unsteady Aerodynamic Modeling for Rotor Aeroelastic Analysis*, Ph.D. thesis, University of Maryland, 2003.

[64]Phanse, Charles, and Sankar, "Efficient Coupled Fluid-Structure Interaction Approach For Analysis of Rotors in Forward Flight," *AHS Conference*, 2006.

[65]Abras, *Enhancement of Aeroelastic Rotor Airload Prediction Methods*, Ph.D. thesis, Georgia Institute of Technology, 2009.

[66]Liu, *Interfacing Comprehensive Rotorcraft Analysis with advanced Aeromechanics and Vortex Wake Models*, Ph.D. thesis, Georgia Institute of Technology, 2008.

[67]Zaki, *Using Tightly-Coupled CFD-CSD Simulation for Rotorcraft Stability Analysis*, Ph.D. thesis, Georgia Institute of Technology, 2012.

[68]Reveles, *Advanced Methods for Dynamic Aeroelastic Analysis of Rotors*, Ph.D. thesis, Georgia Institute of Technology, 2014.

[69]Ickes, *Improved Helicopter Rotor Performance Prediction Through Loose and Tight CFD-CSD Coupling*, Master's thesis, University of Toledo, 2014.

[70]Marpu, *Physics Based Prediction of Aeromechanical Loads For UH-60A Rotor*, Ph.D. thesis, Georgia Institute of Technology, 2013.

[71]Bhagwat, Ormiston, Saberi, and Xin, "Application of CFD-CSD Coupling for Analysis of Rotorcraft Airloads and Blade Loads in Maneuvering Flight," *AHS Forum*, 2007.

[72]Rajmohan, Manivannan, Sankar, Costello, and Bauchau, "Development of a Methodology for Coupling Rotorcraft Aeromechanics and Vehicle Dynamics to study Helicopters in Maneuvering Flight," *AHS Forum*, 2009.

[73]Morillo, Summers, and Bridgeman, "Implementation of Dymore (CSD)-Overflow-2(CFD) Loose Coupling Methodology at BHTI," *AHS Forum*, 2010.

[74]Min, Agarwal, Wilbur, Smith, Modarres, Zhao, Wong, and Wake, "Toward Improved UH-60A Blade Structural Loads Correlation," *AHS Forum*, 2018.

[75]Hsu and Peters, "Coupled Rotor-Airframe Vibration Analysis by a Combined Harmonic-Balance Impedance-Matching Method," *AHS Forum*, 1980.

[76]Gabel and Sankewitsch, "Rotor-Fuselage Coupling by Impedance," *American Helicopter Society Annual Forum*, 1986.

[77]Staley and Sciarra, "Coupled Rotor-Airframe Vibration Prediction Methods," *American Helicopter Society-NASA Ames Specialists Meeting*, 1971.

[78]Abhishek, Chopra, Purekar, Wang, Phan, Semidey, and Liebshutz, "Rotor Load Prediction using Coupled Rotor-Fuselage Model and Sensor Data," *AHS Forum*, 2012.

[79]Yeo and Chopra, "Coupled Rotor-Fuselage Vibration Analysis Using Detailed 3-D Airframe Models," *Mathematical and Computer Modelling*, 2001.

[80]Bielawa, *Rotary Wing Structural Dynamics and Aeroelasticity*, AIAA, 2006.

[81]Hollrock, "Blade Retention Bearing for Helicopter Rotor," 1981.

[82]Rybicki, "The Sikorsky Elastomeric Rotor," *Journal of the American Helicopter Society*, 1981.

[83]Bousman, "Aerodynamic Characteristics of SC1095 and SC1094 R8 Airfoils," Tech. rep., NASA, 2003.

[84]Miao and Mouzakis, "Nonlinear Dynamic Characteristics of the Rotor Bifilar Absorber," *AHS Forum*, 1981.

[85]Bauchau, Rodriguez, and Chen, "Modeling the Bifilar Pendulum Using Nonlinear Flexible Multibody Dynamics," *Journal of the American Helicopter Society*, 2003.

[86]Duh and Miao, "Development of Monofilar Rotor Hub Vibration Absorber," Tech. rep., NASA Contractor Report, 1983.

[87]Abhishek, Datta, and Chopra, "Prediction of UH-60A Structural Loads Using Multibody Analysis and Swashplate Dynamics," *Journal of Aircraft*, 2009.

[88]Yeo, Truong, and Ormiston, "Asessment of 1D Versus 3D Methods for Modeling Rotor Blade Structural Dynamics," *AIAA Conference*, 2010.

[89]Peters and He, "Finite State Induced Flow Models Part II - Three-Dimensional Rotor Disk," *Journal of Aircraft*, 1995.

[90]Ho, Yeo, and Ormiston, "Investigation of Rotor Blade Structural Dynamics and Modeling Based on Measured Airloads," *AHS Forum*, 2007.

[91]Sitaraman and Roget, "Prediction of Helicopter Maneuver Loads Using a Fluid-Structure Analysis," *Journal of Aircraft*, 2009.

[92]Wachspress, Quackenbush, and Boschitsch, "First-Principles Free-Vortex Wake Analysis for Helicopters and Tiltrotors," *AHS Forum*, 2003.

[93]Yeo, Bousman, and Johnson, "Performance Analysis of a Utility Helicopter with Standard and Advanced Rotors," *Journal of the American Helicopter Society*, 2004.

[94]Ormiston, "An Investigation of the Mechanical Airloads Problem for Evaluating Rotor Blade Structural Dynamics Analysis," *AHS Forum*, 2004.

[95]Cronkhite, "Development, Documentation and Correlation of a NASTRAN Vibration Model of the AH-1G Helicopter Airframe," 1976.

[96]Dompka and Cronkhite, "Summary of AH-1G Flight Vibration Data For Validation of Coupled Rotor-Fuselage Analysis," Tech. rep., NASA Contractor Report, 1986.

[97]Murthy, "Design Sensitivity Analysis of Rotorcraft Airframe Structures for Vibration Reduction," *NASA*, 1987.

[98]Hilbert, "A Mathematical Model of the UH-60 Helicopter," Tech. rep., NASA Technical Memorandum, 1984.

[99]Johnson, "NDARC - NASA Design and Analysis of Rotorcraft, Validation and Demonstration," *AHS Specialists Conference*, 2010.

[100]Haeussler, Klaassen, and Rixen, "Comparison of Substructering Techniques for Experimental Identification of Rubber Isolators Dynamic Properties," 2018.

[101]Yeo, "UH-60A Rotor Structural Loads Analysis with Fixed-System Structural Dynamics Modeling," *AHS Forum*, 2018.

[102]Datta, Sitaraman, Baeder, and Chopra, "Analysis Refinements for Prediction of Rotor Vibratory Loads in High-Speed Forward Flight," *American Helicopter Society Annual Forum*, 2004.

[103]Coleman and Bousman, "Aerodynamic Limitations of the UH-60A Rotor," Tech. rep., NASA Technical Report, 1996.

[104]Yeo and Johnson, "Assessment of Comprehensive Analysis Calculation of Airloads on Helicopter Rotors," *AHS Forum*, 2004.

[105]Yeo and Potsdam, "Rotor Structural Loads Analysis Using Coupled Computational Fluid Dynamics-Computational Structural Dynamics," *AHS Forum*, 2014.

[106]Potsdam, Yeo, and Johnson, "Rotor Airloads Prediction Using Loose Aerodynamic-Structural Coupling," *Journal of Aircraft*, 2006.

[107]Ho and Yeo, "Assessment of Comprehensive Analysis Predictions of Helicopter Rotor Blade Loads in Forward Flight," *AHS Forum*, 2016.

[108]Chang, Romander, Potsdam, and Yeo, "Air-Loads Prediction of a UH-60A Rotor inside the 40- by 80-Foot Wind Tunnel," *American Helicopter Society Aeromechanics Specialist Conference*, 2010.

[109]Biedron and Lee-Rausch, "Computation of UH-60A Airloads Using CFD-CSD Coupling On Unstructured Meshes," *AHS Forum*, 2011.

[110]Johnson, *Rotorcraft Aeromechanics*, Cambridge University Press, 2013.

[111]Oberinger, *Modellbildung und Berechnung von Rotor-Zelle Kopplungserscheinungen am Hubschrauber und deren Interpretation mittels Energieflussmethoden*, Ph.D. thesis, Technical University of Munich, 2016.

[112]Coe, "Comparison of Predicted and Measured Temperatures of UH-60A Helicopter Transmission," Tech. rep., NASA, AVSCOM, 1989.

[113]Bauchau and Rodriguez, "Formulation of Modal Based Elements in Nonlinear, Flexible Multibody Dynamics," *Journal of Multiscale Computational Engineering*, 2003.

[114]Saberi, Hasbun, Blumenstein, and Kim, "Coupling of Rotorcraft Elastic Fuselage with CFD," *AHS Forum*, 2018.

[115]Buckanin and Kelly, "Level Flight Performance Evaluation of the UH-60A Helicopter with the Production External Stores Support System and Ferry Tanks Installed," Tech. rep., USAAEFA, 1986.

[116]Cross, Brilla, Kufeld, and Balough, "The Modern Rotor Aerodynamic Limits Survey - A Report and Data Survey," Tech. rep., NASA, 1993.

[117]Murrell, Herbst, Skinner, and Cripps, "Flight Evaluation of the UH-60A Helicopter with the Pitch Bias Actuator Centered and Electrically Disconnected," Tech. rep., US Army, 1986.

[118]Peters, Chouchane, and Fulton, "Helicopter Trim with Flap-Lag-Torsion and Stall by an Optimized Controller," *Journal of Guidance*, 1990.

[119]Guo, *Flight Control Design for Rotorcraft with variable Rotor Speed*, Ph.D. thesis, The Pennsylvania State University, 2009.

[120]Peters and Barwey, "A General Theory of Rotorcraft Trim," *MPE*, 1996.

[121]Norman, Peterson, Maier, and Yeo, "Evaluation of Wind Tunnel and Scaling Effects with the UH-60A Airloads Rotor," *AHS Forum*, 2011.

[122]Kufeld and Johnson, "The Effects of Control System Stiffness Models on the Dynamic Stall Behavior of a Helicopter," *Journal of the American Helicopter Society*, 2000.

[123]Olson, Abrego, Barrows, and Burner, "Blade Deflection Measurements of a Full-Scale UH-60A Rotor System," *American Helicopter Society Aeromechanics Specialist Conference*, 2010.

[124]Arcidiacono and Zincone, "Titanium UTTAS Main Rotor Blade," *American Helicopter Society Annual Forum*, 1975.

[125]Shinoda, Jacklin, Yeo, Bernhard, and Haber, "Investigation of a Full-Scale Wide Chord Blade Rotor System in the NASA Ames 40- by 80-Fuut Wind Tunnel," *American Helicopter Society Specialists Conference on Aeromechanics*, 2004.

Appendix

	symbol	value	description
general	N_b	4	[15, 17, 20, 36, 47, 98, 99]
	σ	0.0826	[15, 17, 20, 48]
	R	8.179 m	[15, 17, 20, 47] [36, 98, 99]
	γ	3°	shaft angle [15, 17, 20, 47, 98]
rotor head &	β_0	8°	precone angle for zero strain [82]
blade attachment	ζ_0	7°	prelag angle for zero strain [22, 82, 121, 122]
	θ_{ref}	8°	built-in pitch angle of .75 R radial station [28]
	e	0.381 m	flap & lag hinge offset [17, 28, 36, 98]
	y_{ph}	0.184 m	pitchhorn distance to feathering axis [28, 36]
	z_{ph}	0.024 m	pitchhorn vertical offset [28]
bifilar absorber	r_{i}	0.4628 m	radial station of inner hole center [86]
	R_{i}	0.0492 m	radius inner hole [86]
	R_{p}	0.0222 m	radius tuning pin [86]
	R_{o}	0.0496 m	radius outer hole, tuned towards 3/rev
	R_{m}	0.0394 m	tuning mass distance to outer hole midpoint [86]
	ϕ_{ba}	45°	azimuthal built-in angle [48]
swash plate	z_{sw}	0.375 m	vertical swashplate position [28]
	r_{pl}	0.442 m	radial position pitchlink pick up [28, 36, 122]
	ϕ_{pl}	31.217°	azimuthal position [17, 36]
	r_{sv}	0.273 m	radial position servo pick up [122]
shaft	l_{sh}	0.5 m	length graphically determined [28]
scissor	z_{sc}	0.214 m	vertical position graphically determined [28]
	$l_{\text{sc,r}}$	0.423 m	scissor hinge radial position calculated [28]
	$l_{\text{sc,v}}$	0.090 m	scissor hinge vertical position calculated [28]
	ϕ_{sc}	30°	azimuthal position estimated from [10]
	$r_{\text{sc,o}}$	0.402 m	outer pick up radius [28]
	$r_{\text{sc,i}}$	0.246 m	inner pick up radius graphically determined [28]
pitch link	l_{pl}	0.405 m	length pitch link [28]
	Θ_{pl}	0.424°	pitch link tilt angle in radial direction, calculated
	Φ_{pl}	0.0°	pitch link tilt angle in azimuthal direction [87]
servos	l_{sv}	0.150 m	servo lenght graphically determined [122]
	ϕ_{sv}	90°	azimuthal orientation of servos [122]
	$\Delta\phi_1$	0°	azimuthal position forward servo [122]
	$\Delta\phi_2$	90°	azimuthal position lateral servo [122]
	$\Delta\phi_3$	180°	azimuthal position aft servo [122]
lag damper	b	0.082 m	B_{ldmr} from [17]
	c	0.306 m	C_{ldmr} from [17]
	d	0.254 m	D_{ldmr} from [17]
	r_{ld}	0.175 m	R_{ldmr} from [17]
	l_{ld}	0.397 m	lag damper length [17]

Table 4: UH-60A main rotor geometry data. Definition of points inherent from figures 28.

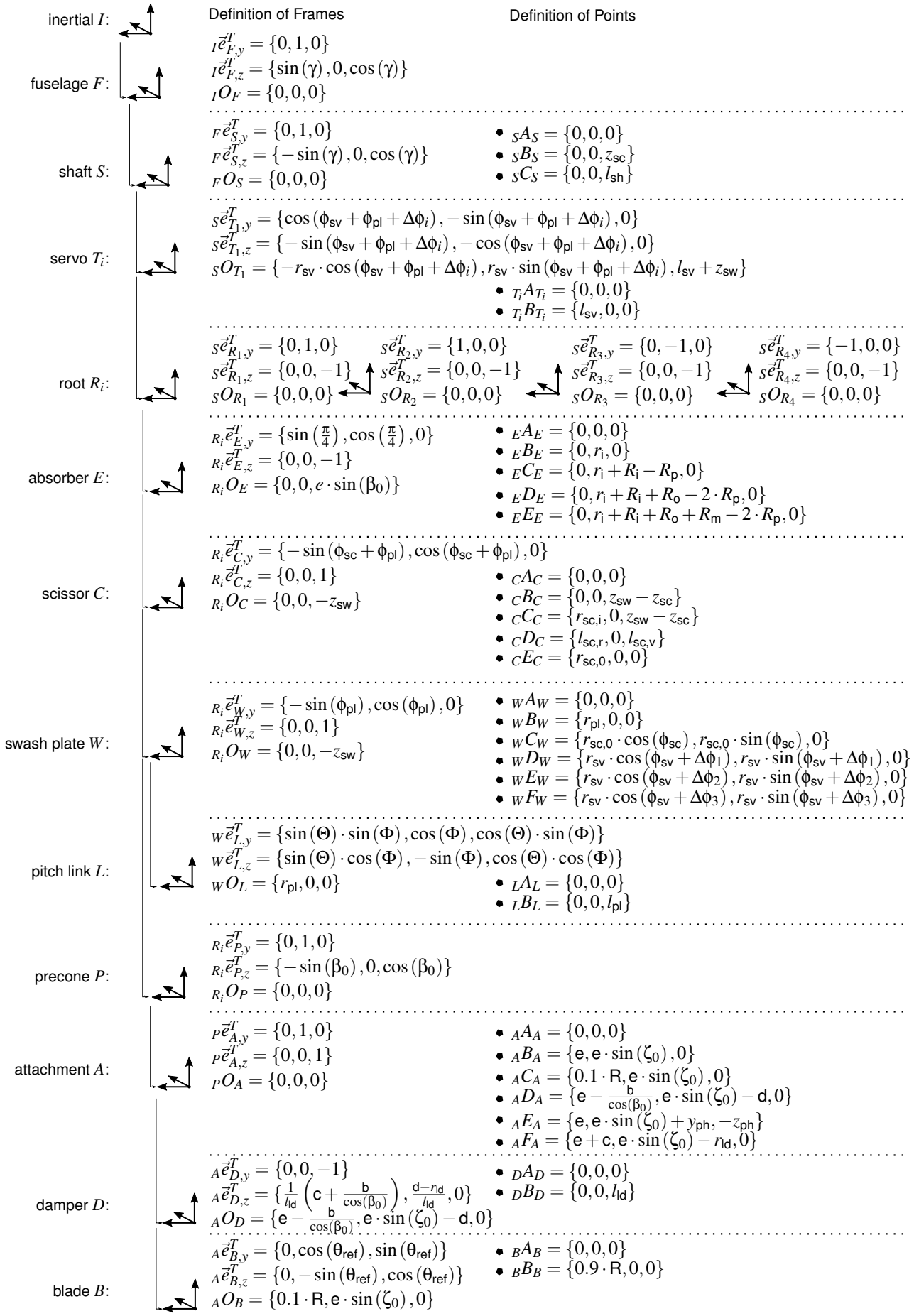

Fig. 8: Definition of frames and points of the rotor system depicted in figure 2. Constants given in table 4. Assumption: $\frac{\cos(\zeta_0)}{\cos(\beta_0)} \approx 1$**.**

	description	comment / value	reference
general	$(C_T/\sigma)_{\max}$ main rotor	0.1846	[98]
	main rotor speed	4.3 Hz	[15, 20, 33, 36, 47, 48, 98, 99]
	lock number main rotor	8.1936	[98, 99]
rotor head &	$^{(*)}$flap/lag hinge stiffness	5250ft-lb/rad	[94]
blade attachment	$^{(*)}$ pitch horn stiffness	8.758+e06N/m	[28]
	$^{(*)}$pitch bearing damping	20(ft-lb)/(rad-sec)	[94]
shaft	stiffness	calculated for a steel cylinder:	
	inner radius r_i	0.09m *(graphically estimated)*	[35]
	outer radius r_o	0.1m *(graphically estimated)*	[35]
damper	damper characteristic		[17]
	associated spring stiffness	0.0N/m	[36]
blade	sectional beam properties		[25, 28]
	structural twist		[10, 17, 123, 124]
	aerodynamic twist		[83]
	2D airfoil tables		[17]
	main rotor profiles	SC1095, SC1094(5)R8	[13, 15, 17, 20, 83]
	airfoil distribution	NO polar: $0.0 - 0.757$m,	[10, 83, 125]
	(linearly interpolated)	SC1095: $0.757 - 2.992$m	
		SC1094R8: $3.246 - 5.913$m	
		SC1095: $6.167 - 7.361$m	
	chord length	data from references consolidated	[28, 83]
	quarter chord offset	data from references consolidated	[25, 28, 83]
bifilar absorber	m_{pin}	2.63kg	[86]
	$m_{\text{tuning mass}}$	15.4kg	[86]
	$I_{\text{z,pin}}$	$0.001952\,\text{kg}\,\text{m}^2$	[86]
	$I_{\text{z,tuning mass}}$	$0.03541\,\text{kg}\,\text{m}^2$	[86]
swash plate	mass	90.54kg	[28]
	diametrical inertia I_{x},I_{y}	$2.054\,\text{kg}\,\text{m}^2$	[28]
pitch link	stiffness	$2.745\text{+e06N}\,\text{m}^{-1}$	[87, 91, 122]
	mass	3.397kg	[28]
	$^{(*)}$ damping	240lb/(ft-sec)	[94]
servos	$^{(*)}$ standalone stiffness	$18.0603\text{+e06N}\,\text{m}^{-1}$	[28]
	forward servo stiffness	$15.0\text{+e06N}\,\text{m}^{-1}$	[87]
	lateral servo stiffness	$4.5\text{+e06N}\,\text{m}^{-1}$	[87]
	aft servo stiffness	$5.8\text{+e06N}\,\text{m}^{-1}$	[87]

$^{(*)}$ *not used in within this work explicitly*

Table 5: UH-60A main rotor structural and aerodynamic properties.

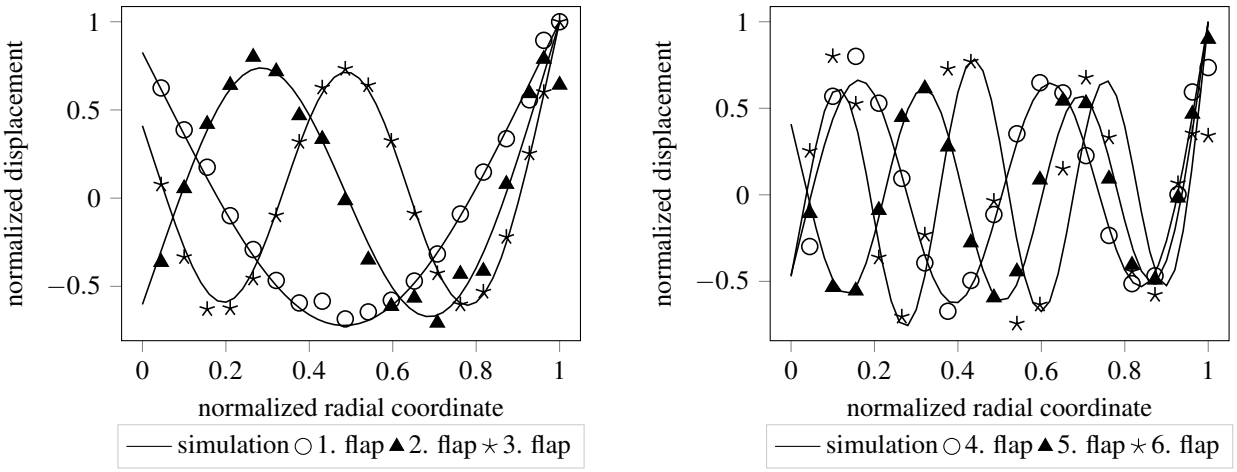

(a) 1.-3. flap modes

(b) 4.-6. flap modes

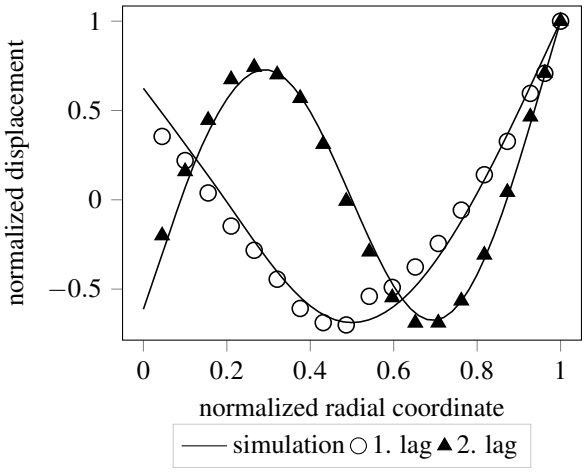

(c) lag modes

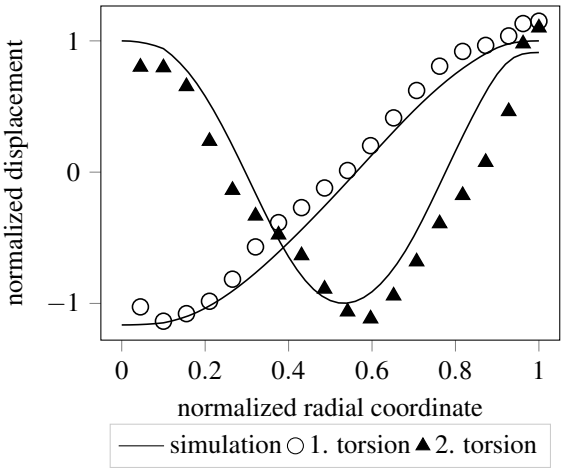

(d) torsion modes

Fig. 9: Comparison of simulated mode shapes with literature [25].

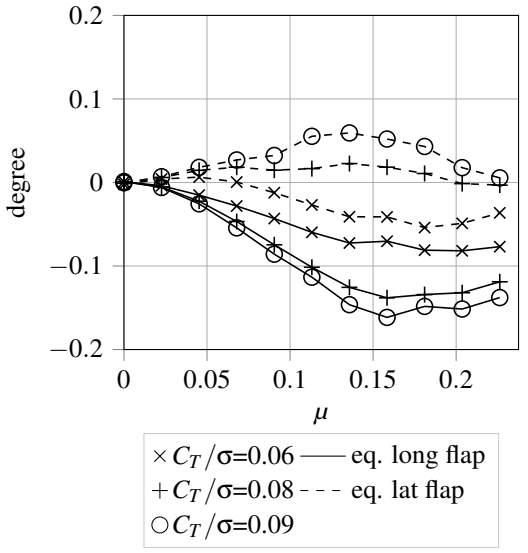

(a) Flap motion.

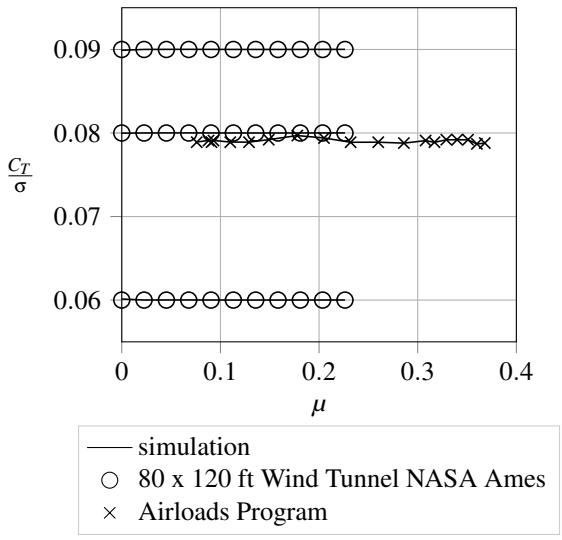

(b) Thrust.

Fig. 10: Simulated UH-60A main rotor states in trimmed condition compared to literature according to Airloads flight test counter 85 [93] and wind tunnel data [30].

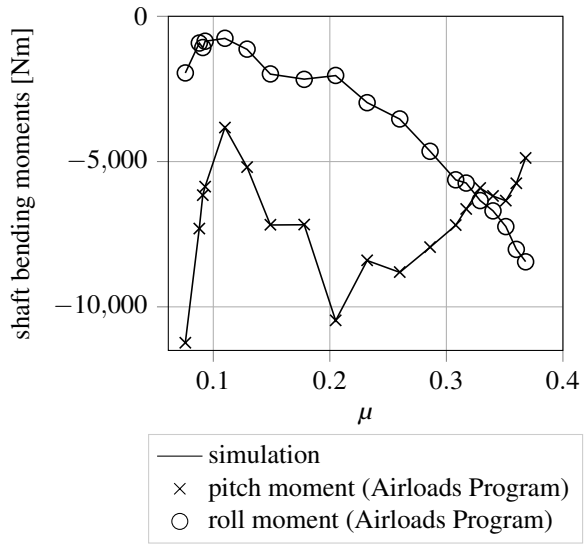

(a) Shaft bending moments.

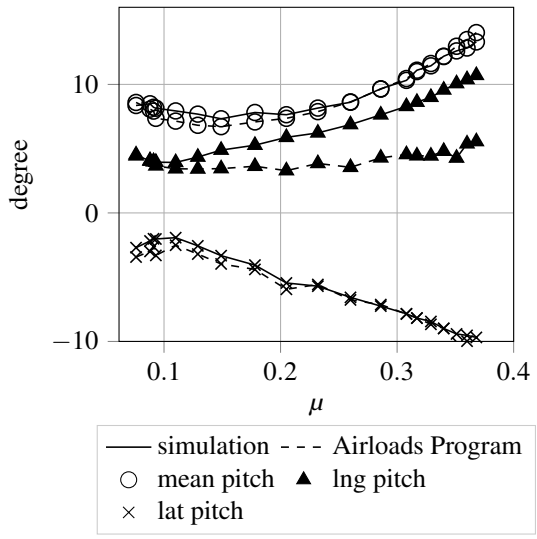

(b) Feathering motion.

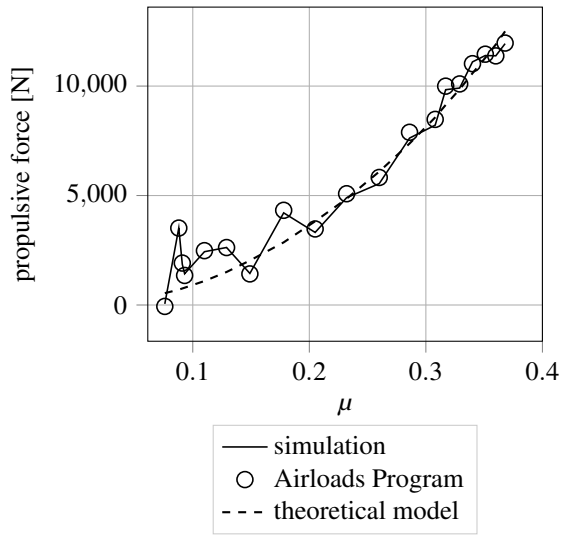

(c) Propulsive main rotor force.

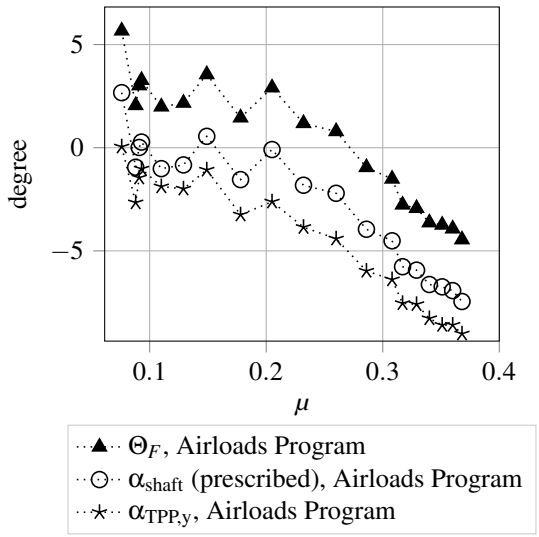

(d) Pitch attitude, shaft and TPP angle.

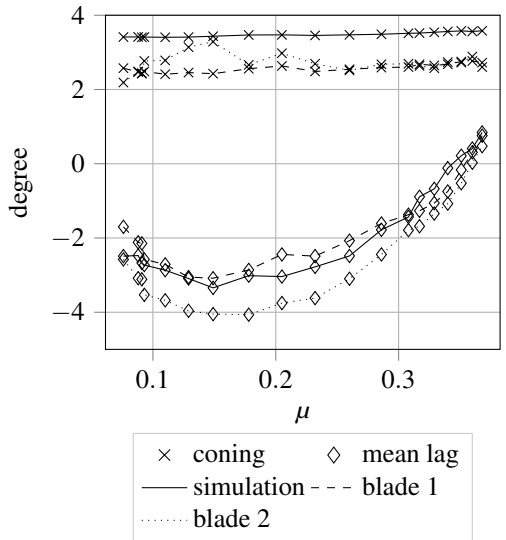

(e) Coning and lead-lag motion.

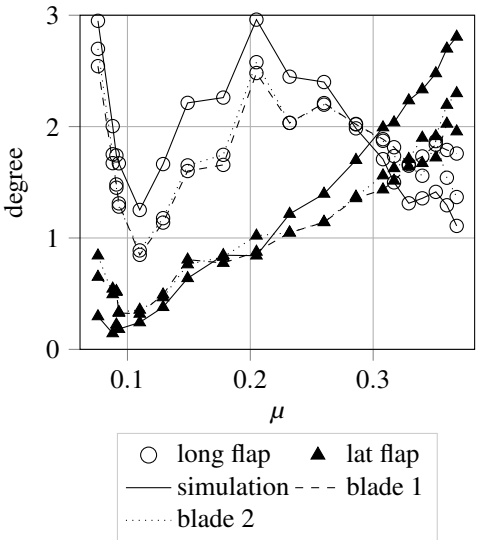

(f) Cyclic flap motion.

Fig. 11: Simulated UH-60A main rotor states in trimmed condition compared to literature according to Airloads flight test counter 85 [93] and wind tunnel data [30].

mode	f [Hz]	D [%]	x y z	r_x r_y r_z
rigid body mode			0.0114572	0
1	0.0	0.0	0	0
			0	0
rigid body mode			0	0
2	0.0	0.0	0.0114572	0
			0	0
rigid body mode			0	0
3	0.0	0.0	0	0
			0.0114572	0
rigid body mode			0	-0.0125743
4	0.0	0.0	0.0231444	0
			0	0
rigid body mode			0.0080462	0
5	0.0	0.0	0	0.0043715
			0.0020679	0
rigid body mode			0	0
6	0.0	0.0	0.0021154	0
			0	-0.0044974
			5.6176e-05	-1.1325e-02
7	5.1	2.5	8.4264e-03	1.0505e-03
			5.6176e-05	3.4660e-03
			-1.4679e-02	-2.0292e-04
8	6.4	2.5	4.3173e-05	-8.8074e-03
			4.7491e-03	4.7491e-04
			2.7109e-03	-2.6566e-03
9	11.6	2.5	-3.5241e-03	-1.0084e-03
			1.1928e-03	-1.2795e-02
			1.2819e-02	-2.6172e-03
10	12.1	2.5	-8.0117e-03	-9.9345e-04
			1.1750e-03	-1.2605e-02
			-1.8321e-02	-1.4356e-02
11	13.8	2.5	6.8361e-03	-5.7423e-03
			-5.0132e-03	-7.8843e-04
			5.0156e-05	2.3975e-02
12	14.3	2.5	2.7084e-02	1.5548e-04
			-5.0156e-05	7.8746e-04
			3.3350e-02	1.7095e-02
13	15.3	2.5	3.3350e-05	-7.0901e-03
			-1.0338e-02	2.0010e-04
			2.4260e-02	-9.3576e-05
14	17.4	2.5	1.8022e-02	3.1539e-02
			4.3322e-03	2.0795e-04
			-1.5058e-03	7.5288e-03
15	21.1	2.5	6.6254e-03	2.5899e-04
			3.0115e-05	-1.5058e-03

Table 6: Modal main rotor hub properties of the rigid and elastic UH-60A fuselage *HUBNODE* configuration observed from literature [37].

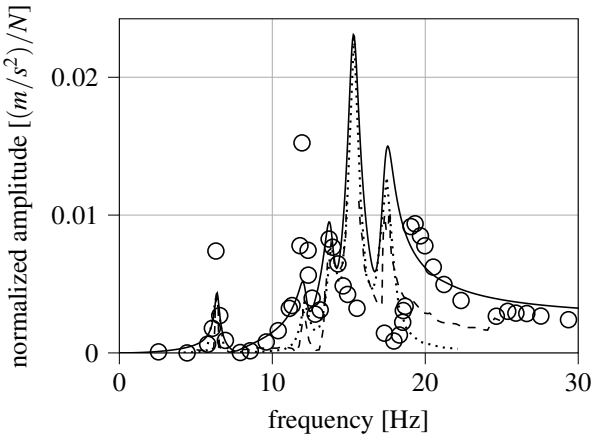

(a) Longitudinal response to longitudinal force.

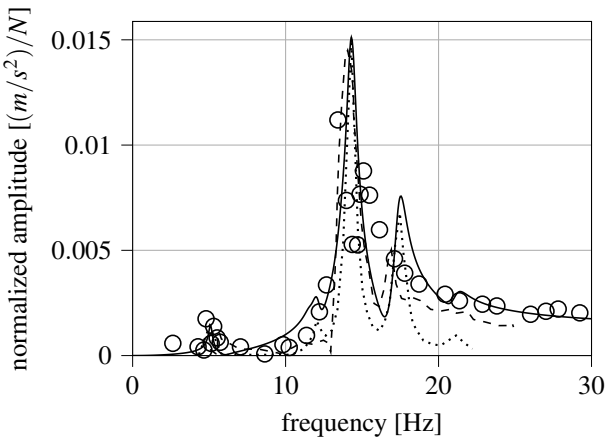

(b) Lateral response to lateral force.

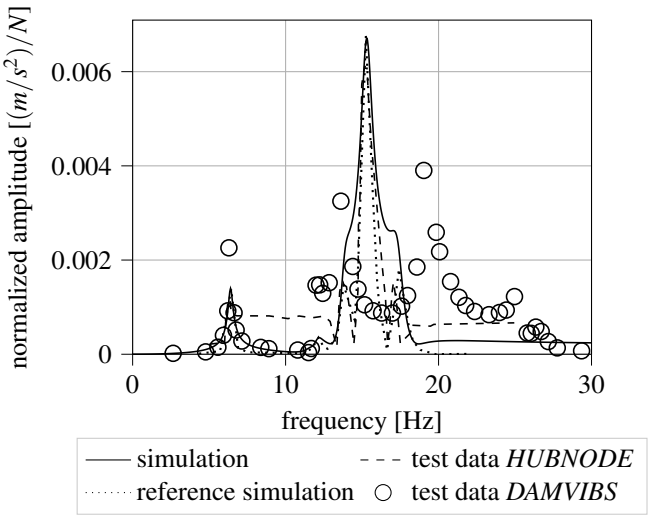

(c) Vertical response to longitudinal force.

Fig. 12: Simulated transfer functions of the UH-60A main rotor hub compared against references [33, 37].

node	direction	mode 1: first lateral bending	mode 2: first vertical bending	mode 3: stabilator rigid body 1	mode 4: transmission pitch	mode 6: transmission roll	mode 5: second vertical bending	mode 7: cockpit cabin roll	mode 8: third vertical bending
	D [%]	1.0	1.0	2.9	1.4	2.7	2.6	2.8	2.1
	ω [Hz]	5.5	(*)6.4	10.1	12.3	13.8	14.0	15.4	19.3
07	y	+4.98e-03	+1.41e-05	-4.46e-03	+7.72e-06	+6.50e-03	+5.69e-04	+0.00e+00	+9.33e-05
	z	+1.12e-03	+8.28e-03	-8.10e-03	+2.74e-03	+2.90e-03	+8.31e-03	-7.01e-03	+2.97e-03
09	x	+0.00e+00	+2.16e-03	-8.46e-03	+1.25e-03	+2.18e-02	+5.29e-04	+1.40e-03	+4.48e-03
	z	+1.19e-03	+7.65e-03	+1.41e-02	+2.68e-03	+0.00e+00	-1.37e-02	+9.09e-03	+2.22e-03
10	y	+5.25e-03	+4.64e-04	-5.35e-03	-1.97e-04	+6.34e-03	-4.14e-04	+0.00e+00	+6.23e-04
	z	-1.79e-03	+7.61e-03	+1.09e-02	+2.07e-03	+3.09e-03	+8.87e-03	+1.04e-02	+1.81e-03
23	x	+0.00e+00	+5.07e-04	+0.00e+00	+8.06e-03	-2.21e-02	-1.42e-03	+0.00e+00	-2.86e-04
	y	-1.32e-03	+1.37e-04	+6.23e-03	+4.83e-04	+1.01e-02	+1.81e-03	+0.00e+00	-9.35e-05
	z	+4.28e-04	+1.06e-03	+4.08e-04	+1.61e-03	-5.52e-03	-1.03e-02	+1.76e-03	+9.14e-03
30	z	+6.85e-04	-1.02e-02	-4.36e-04	-8.34e-03	-3.74e-03	-6.80e-03	+1.71e-03	+1.62e-02
31	y	-3.80e-03	+5.68e-04	-4.71e-03	+1.12e-03	-2.40e-02	-8.40e-04	-1.47e-03	+1.08e-03
	z	-3.27e-04	-6.46e-03	+1.47e-03	-7.02e-03	+3.49e-03	-4.08e-03	-2.27e-03	+5.31e-03
33	y	-5.73e-03	+5.00e-04	+9.36e-03	+2.64e-04	+3.20e-03	-4.64e-04	+0.00e+00	+2.02e-03
	z	+2.14e-03	-1.06e-02	+5.46e-03	-7.90e-03	+4.94e-03	+3.89e-03	-5.36e-03	-1.60e-02
36	z	-1.14e-03	-1.02e-02	+8.50e-03	-8.36e-03	-4.95e-03	-5.82e-03	+4.19e-03	-1.85e-02
55	x	-3.98e-05	+3.11e-03	+2.74e-03	+1.17e-03	+1.92e-03	+2.69e-03	+2.46e-03	+2.97e-03
	y	-3.52e-03	+5.26e-04	+0.00e+00	+2.06e-03	+2.59e-02	+0.00e+00	-2.63e-02	+1.06e-03
	z	-2.42e-04	-1.10e-03	+4.50e-03	+2.16e-02	-1.39e-03	+1.44e-02	-2.63e-04	-1.22e-03
57	x	+5.17e-04	-2.40e-02	-3.06e-03	-1.55e-02	+1.76e-03	-1.03e-02	-1.51e-03	+2.68e-03
	y	+1.54e-02	+0.00e+00	+0.00e+00	+1.18e-03	+1.27e-02	-8.97e-04	+1.54e-02	-1.41e-04
59	x	-2.61e-03	-4.99e-02	+6.08e-03	+3.88e-02	-1.47e-03	+2.35e-02	-3.99e-03	+4.61e-03
	y	+3.52e-02	+0.00e+00	+0.00e+00	+9.60e-04	-1.84e-02	+0.00e+00	-2.11e-02	+3.84e-04
	z	+4.37e-03	+2.72e-02	+5.72e-03	+2.90e-03	+3.84e-03	+6.09e-03	-3.87e-03	+2.47e-03
60	x	-1.25e-02	-1.45e-02	+1.12e-01	+1.01e-02	+6.05e-02	-3.77e-03	+5.13e-02	-2.77e-03
	y	+6.70e-03	+0.00e+00	+0.00e+00	+0.00e+00	+5.67e-02	+0.00e+00	+4.31e-02	+0.00e+00
	z	-2.96e-02	+1.81e-02	-1.46e-01	+3.72e-02	-6.10e-02	-2.79e-02	-1.63e-02	+1.10e-02
62	x	-3.32e-04	-1.05e-02	+1.08e-03	-2.28e-03	+3.92e-03	+3.87e-03	+4.70e-03	-2.37e-03
	z	+2.02e-04	+1.78e-02	+3.26e-03	+1.19e-02	-1.77e-03	+1.28e-02	-1.38e-03	+3.18e-03
64	x	+1.45e-02	-3.30e-03	-1.15e-01	-9.13e-03	-5.33e-02	+8.75e-03	-4.64e-02	+8.37e-03
	y	-3.44e-03	+0.00e+00	+0.00e+00	+2.95e-04	+1.73e-02	+0.00e+00	+1.43e-02	+3.40e-03
	z	+3.24e-02	+1.68e-02	+1.64e-01	+8.49e-03	+5.43e-02	+3.04e-02	+1.65e-02	+1.08e-02
65	x	-6.18e-04	+1.25e-02	-1.72e-03	+2.04e-02	-1.59e-03	+1.85e-02	+1.56e-03	-1.95e-02
	y	-5.94e-03	-3.01e-04	+4.21e-03	-1.68e-03	+2.25e-02	+1.97e-04	-2.13e-02	+6.29e-04
	z	+1.60e-04	-2.52e-03	+9.02e-04	-2.03e-03	+3.02e-03	-1.18e-02	-1.45e-03	+8.57e-03
66	x	+1.22e-04	-5.72e-04	+1.88e-03	-9.11e-03	+9.01e-05	+3.05e-03	+3.39e-04	-8.60e-04
	y	-3.33e-03	+1.87e-04	+7.14e-03	+9.46e-04	+1.09e-02	+2.01e-03	+0.00e+00	+2.14e-04
	z	-1.40e-04	-3.15e-03	+2.20e-04	+1.80e-03	+1.03e-03	-8.26e-03	-3.23e-04	+9.36e-03
72	x	-3.16e-03	-4.73e-02	+6.63e-03	+4.73e-02	-3.18e-03	+3.03e-02	-9.40e-04	+7.74e-03
	y	+3.71e-02	+0.00e+00	+0.00e+00	+0.00e+00	-2.08e-02	+0.00e+00	-2.47e-02	+2.17e-03
	z	-1.78e-02	+3.36e-02	+7.48e-03	+7.41e-03	+1.33e-02	+5.23e-04	-1.41e-02	-1.11e-03

node 07:	pilot floor	node 33:	rear cabin floor right	node 62:	horizontal tail mid
node 09:	copilot floor right	node 36:	rear cabin floor left	node 64:	horizontal tail left tip
node 10:	copilot floor left	node 55:	vertical tail bottom	node 65:	main rotor shaft top
node 23:	control linkage forward	node 57:	vertical tail mid	node 66:	main rotor shaft bottom
node 30:	control linkage aft right	node 59:	vertical tail top	node 72:	tail rotor hub
node 31:	control linkage aft left	node 60:	horizontal tail right tip	***NOTE:***	*masses scaled to unity*

(*) *this value is changed with regard to* [33] *for better agreement with experimental data and other references* [36]

Table 7: Identified fuselage modes based on literature [33]. Note that the zeros elements have been set manually after minimizing the objective function 19 for better visual agreement of the mode shapes.

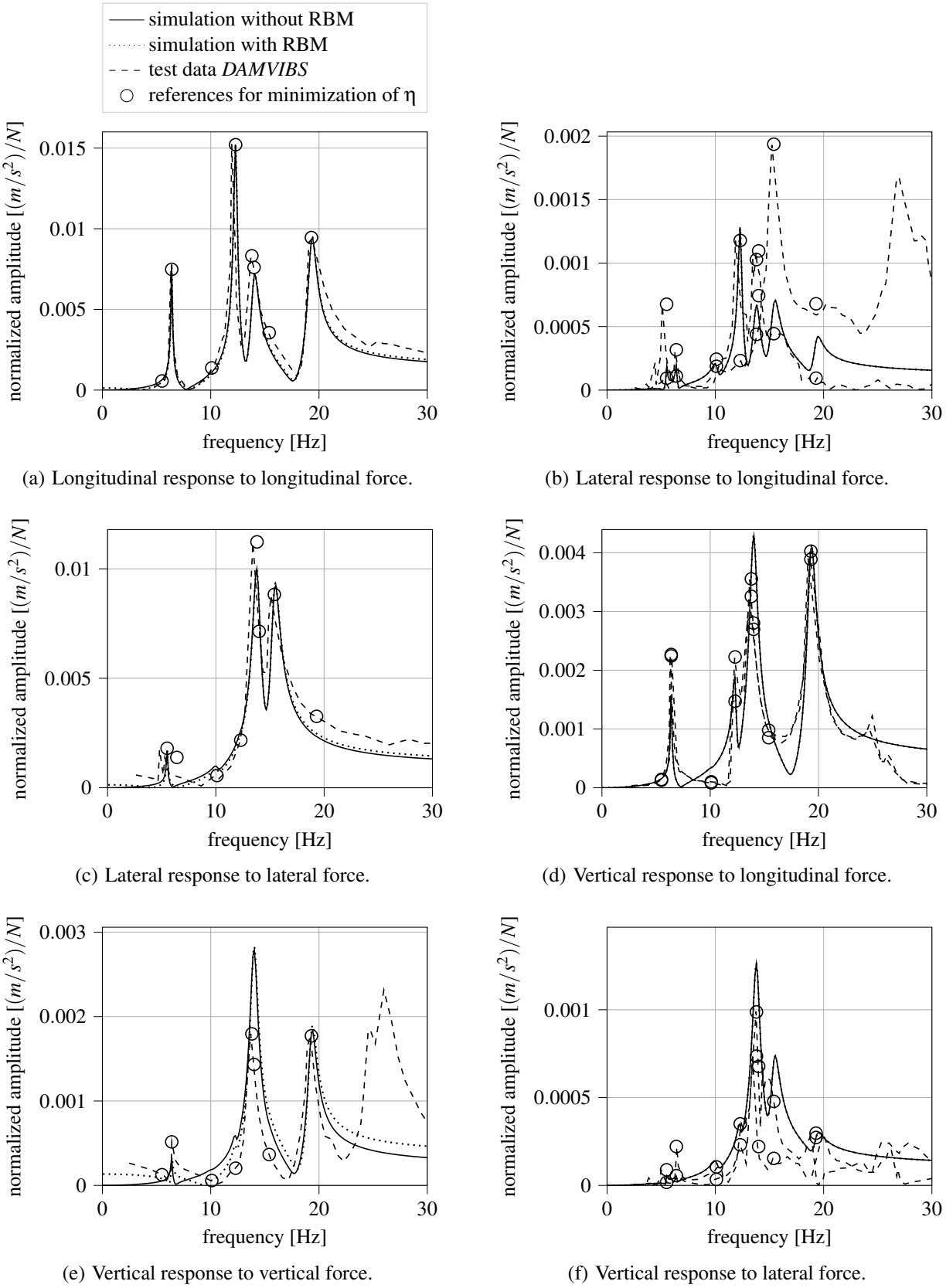

(a) Longitudinal response to longitudinal force.

(b) Lateral response to longitudinal force.

(c) Lateral response to lateral force.

(d) Vertical response to longitudinal force.

(e) Vertical response to vertical force.

(f) Vertical response to lateral force.

Fig. 13: Simulated transfer function of the UH-60A main rotor hub with and without rigid body modes compared against literature [33].

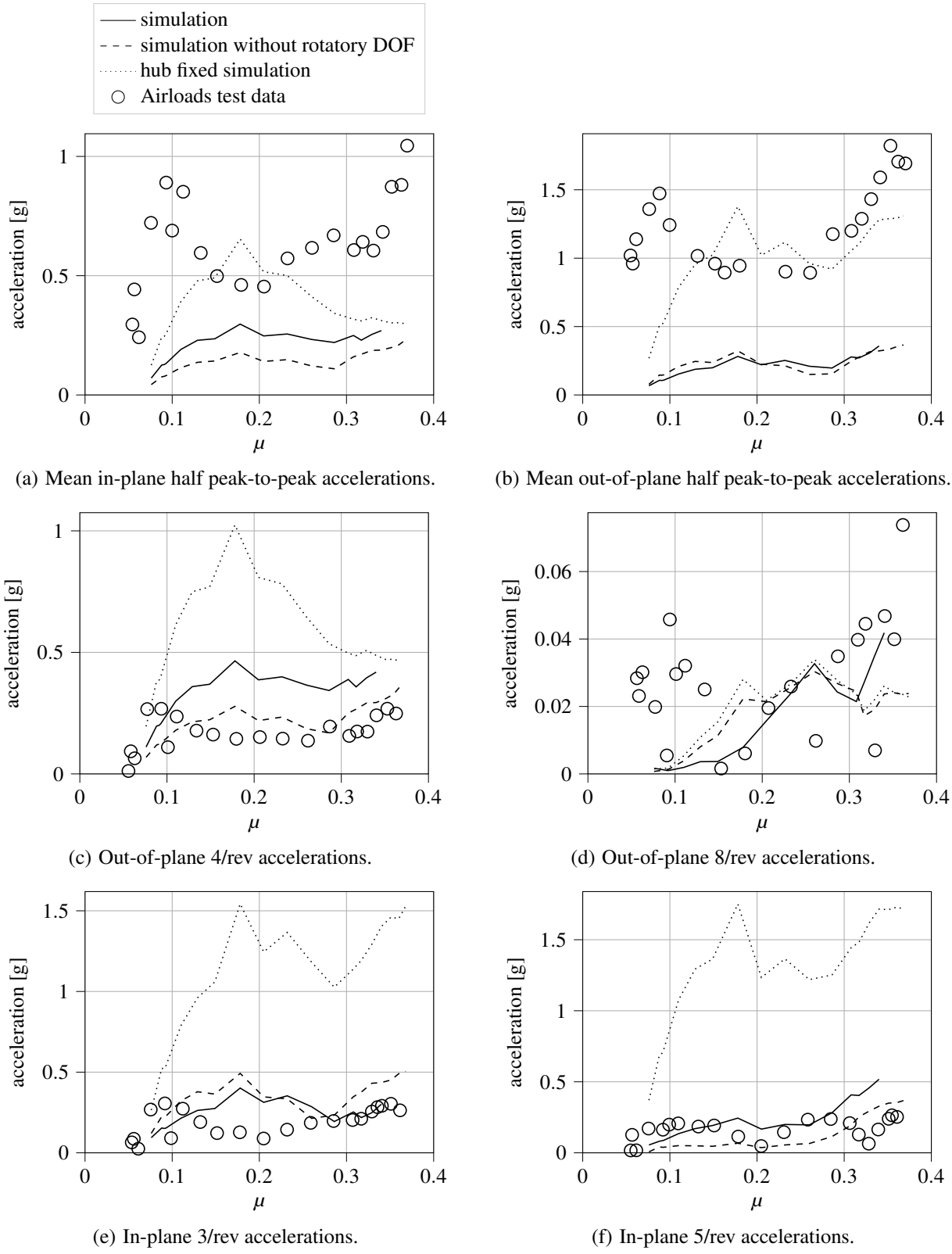

(a) Mean in-plane half peak-to-peak accelerations.

(b) Mean out-of-plane half peak-to-peak accelerations.

(c) Out-of-plane 4/rev accelerations.

(d) Out-of-plane 8/rev accelerations.

(e) In-plane 3/rev accelerations.

(f) In-plane 5/rev accelerations.

Fig. 14: UH-60A hub accelerations in trimmed horizontal edgewise flight. According to Airloads flight test counter 85 velocity sweep [22, 93]. *HUBNODE* configuration used to represent the fuselage.